

# *Facies and Reservoir-quality Variations in the Late Visean to Bashkirian Outer Platform, Rim, and Flank of the Tengiz Buildup, Precaspian Basin, Kazakhstan*

**J. F. Collins**

*ExxonMobil Development Company,  
Houston, Texas, U.S.A.*

**J. A. M. Kenter<sup>1</sup>**

*Vrije University, Amsterdam, Netherlands*

**P. M. Harris**

*Chevron Energy Technology Company,  
San Ramon, California, U.S.A.*

**G. Kuanysheva**

*TengizChevroil, Atyrau, Kazakhstan*

**D. J. Fischer**

*TengizChevroil, Atyrau, Kazakhstan*

**K. L. Steffen**

*ExxonMobil Development Company,  
Houston, Texas, U.S.A.*

## ABSTRACT

**T**engiz field is an isolated carbonate buildup in the southeastern Precaspian Basin, containing a succession of shallow-water platforms ranging in age from late Famennian to early Bashkirian. Platform backstepping from Tournaisian through late Visean resulted in approximately 800 m (2625 ft) of bathymetric relief above the Famennian platform. This was followed by as much as 2 km (1.2 mi) of Serpukhovian progradation, which formed a depositional wedge around the older platforms referred to as the Serpukhovian rim and flank.

Rim and flank facies include lower slope mudstone, volcanic ash, and platform-derived skeletal packstone to grainstone interbedded with boundstone breccia; middle-slope poorly bedded to massive boundstone breccia with subtypes based on clast composition, size, and packing; upper-slope in-situ microbial boundstone; and outer-platform to shallow-platform skeletal, coated-grain, and ooid packstone to grainstone. The upper-slope microbial boundstone represents the

<sup>1</sup>Present address: Chevron Energy Technology Company, San Ramon, California, U.S.A.

dominant source of clasts in the middle- and lower-slope breccias. Periodic large-scale failure of the rim during both Serpukhovian and Bashkirian time resulted in a high degree of lateral facies discontinuity.

Solution-enlarged fractures, large vugs, and lost circulation zones produced mainly during late diagenesis form a high-permeability, well-connected reservoir in the rim and flank. This diagenetic overprint is associated with the presence of bitumen and extends upward into overlying Serpukhovian and Bashkirian platform facies and inward into adjacent late Visean platforms, where it has substantially altered reservoir properties that remained after early diagenesis related to cyclic depositional processes.

## INTRODUCTION

The Tengiz field is located in onshore western Kazakhstan at the northern end of the Caspian Sea's eastern shoreline, among an archipelago of isolated carbonate buildups that grew on a regional pre-Middle Devonian structural high (Figure 1). Tengiz was discovered in 1979 by the Oil Ministry of the former Soviet Union and, since 1993, has been operated by TengizChevroil (TCO), an in-country joint-venture company. The field is covered by a three-dimensional (3-D) seismic survey encompassing about 1000 km<sup>2</sup> (385 mi<sup>2</sup>), acquired in 1998. As of year-end 2005, more than 115 wells have penetrated the reservoir at Tengiz (Figure 2), which produces an intermediate sulfur oil (47° API). The highest initial production rates are from wells located in the buildup rim and flank areas, in fractured carbonates with low (<6%) matrix porosity. Wells located toward the center encounter higher porosity (as much as 18%) but lower matrix permeability (<10 md) and lower initial rates.

The Tengiz buildup formed sometime after the Middle Devonian and grew more or less uninterrupted until the early Bashkirian by aggradation of a series of grain-dominated platforms. The total thickness of carbonate is unknown, but is represented by approximately 1.2 s TWT on 3-D seismic data. The deepest borehole to date bottomed in the middle Famennian at 6032 m (19,790 ft) subsea, more than 2100 m (6890 ft) below the top of the reservoir and more than 700 m (2297 ft) below the top of the Famennian platform. Following platform demise in the Bashkirian, the Tengiz buildup was buried initially by a thin veneer of Moscovian through Artinskian carbonates and volcanoclastics and then by thick Kungurian evaporites (mainly halite) that completely encased the platform. Post-Permian salt diapirism produced a series of salt pillars and clastic-filled withdrawal basins above the platforms, which locally adversely affect 3-D seismic image quality (Figure 3A).

## STRATIGRAPHY

In 2001, a joint study by ExxonMobil, Chevron, and TCO established a stratigraphic framework for the Tengiz platform based on seismic, biostratigraphic, core, and well-log data that existed up to that time. This study was published (Weber et al., 2003) and stands as the definitive stratigraphic reference for Tengiz. The published framework includes a hierarchy of second-order, third-order, and fourth-order sequences that have been maintained as Tengiz drilling proceeds. This architecture is a locally applicable, fit-for-purpose framework, although it more or less conforms to the second-order eustatic cycles of Ross and Ross (1987).

This chapter describes facies and reservoir-quality variations in the Visean A through Bashkirian platform margins at Tengiz (Figure 3B). This interval forms the late highstand of a second-order supersequence set that began with deposition of a series of backstepping platforms in the Tournaisian. By the end of the Visean, the platform area had decreased from 210 km<sup>2</sup> (81 mi<sup>2</sup>) in the late Famennian to about 90 km<sup>2</sup> (35 mi<sup>2</sup>). During the Serpukhovian, the Tengiz platform prograded as much as 2 km (1.2 mi) basinward, filling much of the accommodation space created during backstepping, and forming a microbial boundstone-cored depositional wedge known as the rim and flank around the late Visean and older platforms. This wedge attained a maximum thickness of more than 800 m (2625 ft). Following a brief depositional hiatus on the platform (Brenckle and Milkina, 2003), early Bashkirian platform carbonates accumulated more or less aggradationally above the Serpukhovian. Because this chapter also discusses reservoir connectivity between the Serpukhovian rim and flank, the overlying Bashkirian outer platform region, and the adjacent Visean A platforms, a brief description of how platform facies correlate to rim and flank facies is included here. For a detailed account of the nature

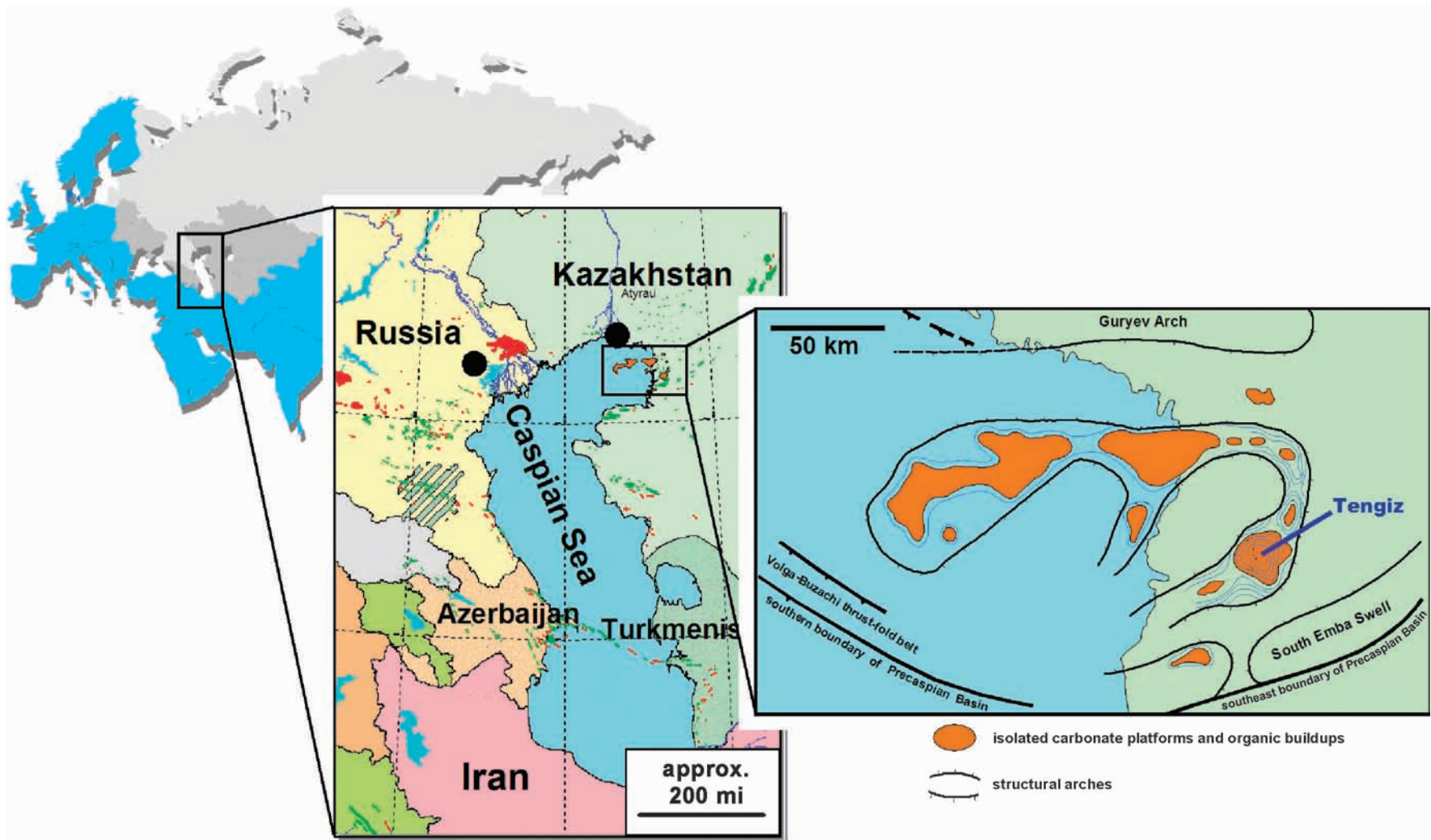


**FIGURE 1.** North Caspian region and location of the Tengiz field.

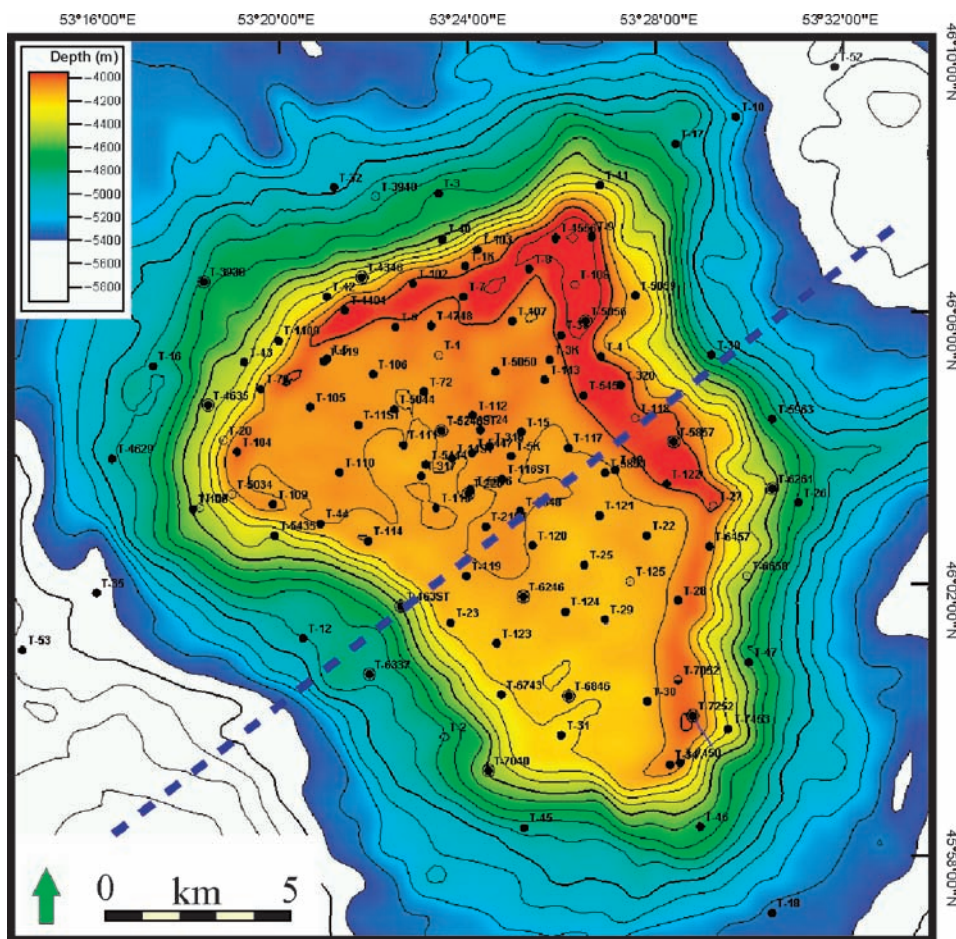


**FIGURE 2.** Structure contours on top of the Tengiz buildup. Current well locations and the path of the seismic profile in Figure 3 are indicated. Contour interval = 100 m (330 ft).

than 10 m (33 ft) to several tens of meters. They consist of dipping, bedded to massive skeletal packstone to rudstone containing abundant large crinoids and brachiopod fragments, minor colonial coral detritus, and occasional platform-derived breccias. In the central platform, fourth-order sequence boundaries are associated with subaerial exposure and deposition of low-energy or restricted facies containing thin volcanic ash layers (Kenter et al., 2006). In the Serpukhovian outer-platform cycles, these features are reduced or absent at the sequence boundaries.

of the Viséan A, Serpukhovian, and Bashkirian central platform regions, the reader is referred to Kenter et al. (2006).

### *Viséan A, Serpukhovian, and Bashkirian Platform Cycles*

Viséan A, Serpukhovian, and Bashkirian fourth-order central platform sequences generally adhere to the model shown in Figure 4. These sequences feature depositional environments ranging from high-energy grainstone shoals to slightly deeper environments characterized by more poorly sorted, open-marine grainstone to packstone, or in some cases, mudstone and faunally restricted, fine-grained carbonate sand. Outer platform cycles vary over the interval but are generally characterized by an increase in algal grains and micritic intraclasts. Because of the unique nature of microbial facies in the rim and flank, greater attention is given to Serpukhovian outer-platform cyclicity. These cycles are commonly poorly expressed and range in thickness from less

## DEPOSITIONAL ENVIRONMENTS

### *General Features of the Tengiz Rim and Flank*

The terms “platform,” “rim,” and “flank” were originally derived from seismic features and are now used for drilling purposes to denote geographic regions in the field. The platform region comprises boreholes that penetrate the stack of backstepping platforms, whereas boreholes that encounter any part of the adjacent progradational wedge are described as rim and flank wells. As mentioned earlier, the wedge arises as a result of Serpukhovian progradation, but includes rocks of Serpukhovian and Bashkirian age (see Figure 3). The rim area refers to the inner, structurally elevated rim crest or raised rim, whereas the flank refers to the outer sloping surface. The raised rim is interpreted to have formed mainly by differential compaction caused by a mechanical contrast between grainy platform facies and more rigid upper-slope microbial boundstone facies in the rim and has resulted in as much as 50 ms of seismic relief and as much as 200–250 m (656–820 ft) of

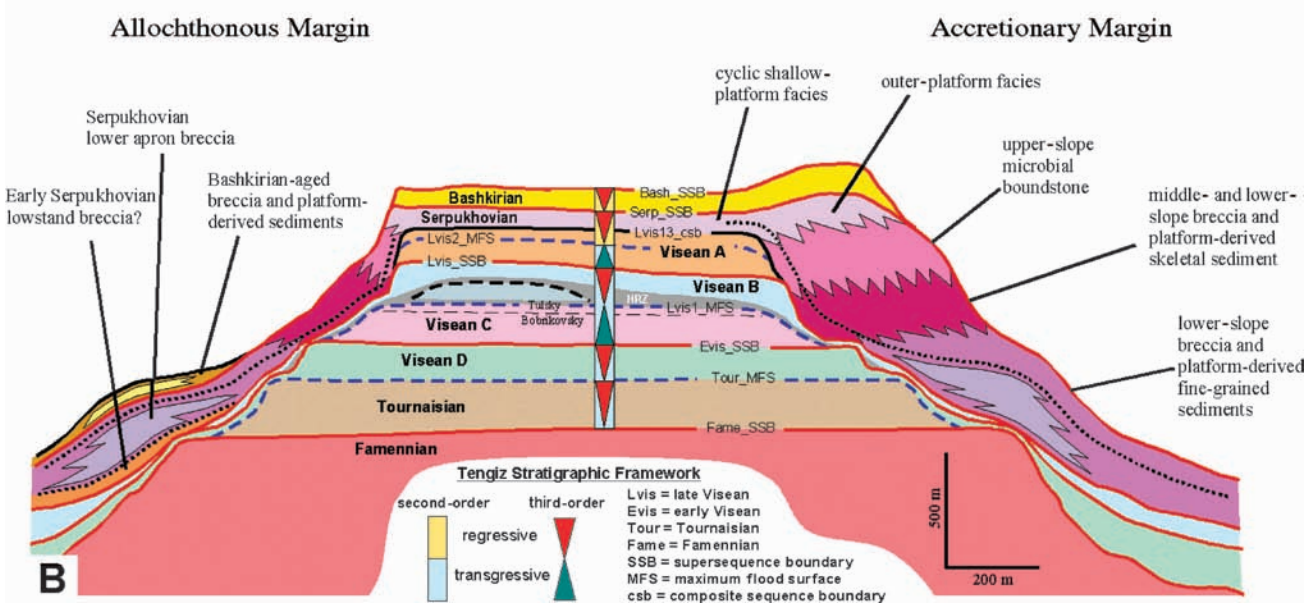
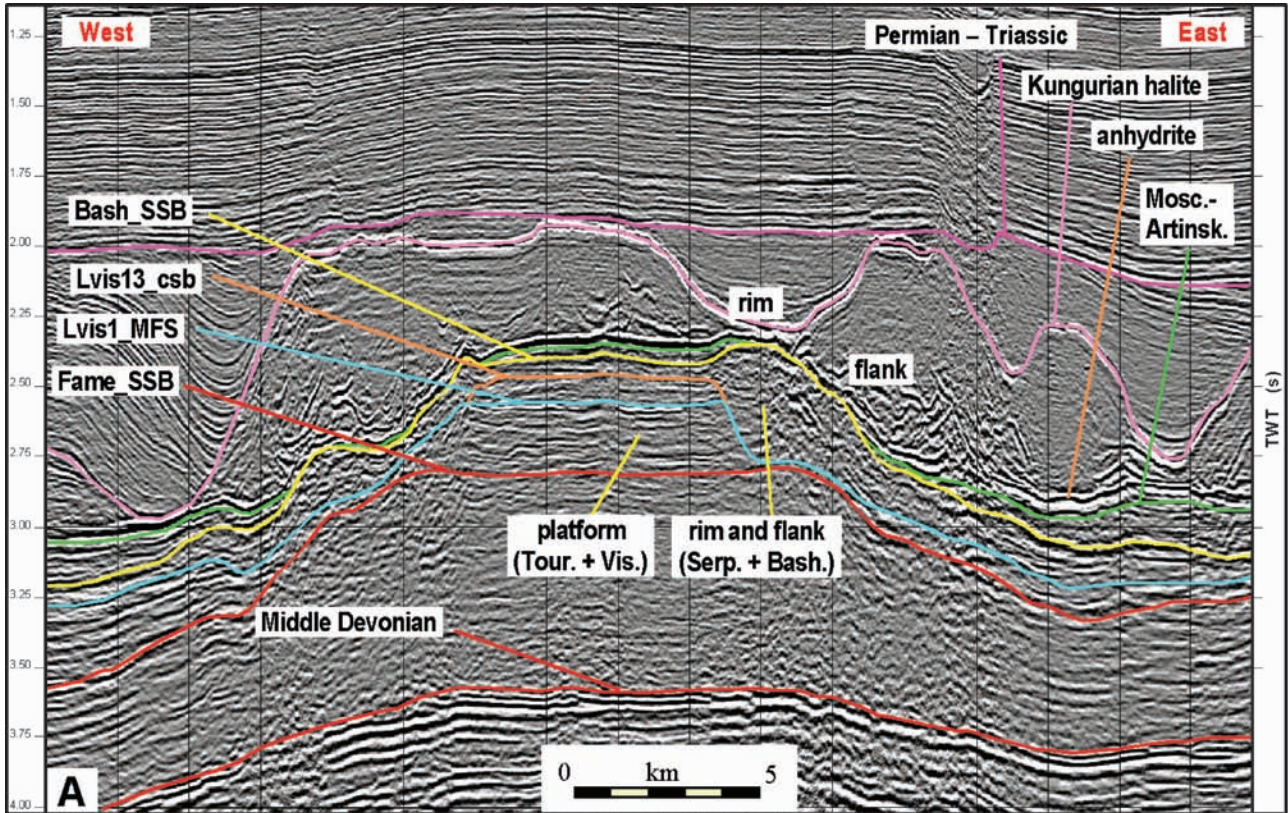


**FIGURE 3.** Tengiz stratigraphic framework and the Serpukhovian rim and flank region. The seismic line (A) shows the east-west asymmetry in the shape of the wedge and in the width of the structurally elevated portion (raised rim). The seismic profile also shows the absence of Moscovian–Artinskian volcanic sediments on the upper flank of the buildup, placing an anhydrite layer at the base of the salt in direct contact with the reservoir, as well as the source rock interval associated with subsalt facies in the same interval in surrounding lows. These are two potentially important factors in rim and flank diagenesis. The schematic framework (B) is derived from Weber et al. (2003), with details from this study added in the rim and flank area. In particular, the diagram shows the rim and flank to consist of an early debris apron that accumulated around the base of the buildup, followed by progradation of a boundstone-cored upper wedge (black dashed line).

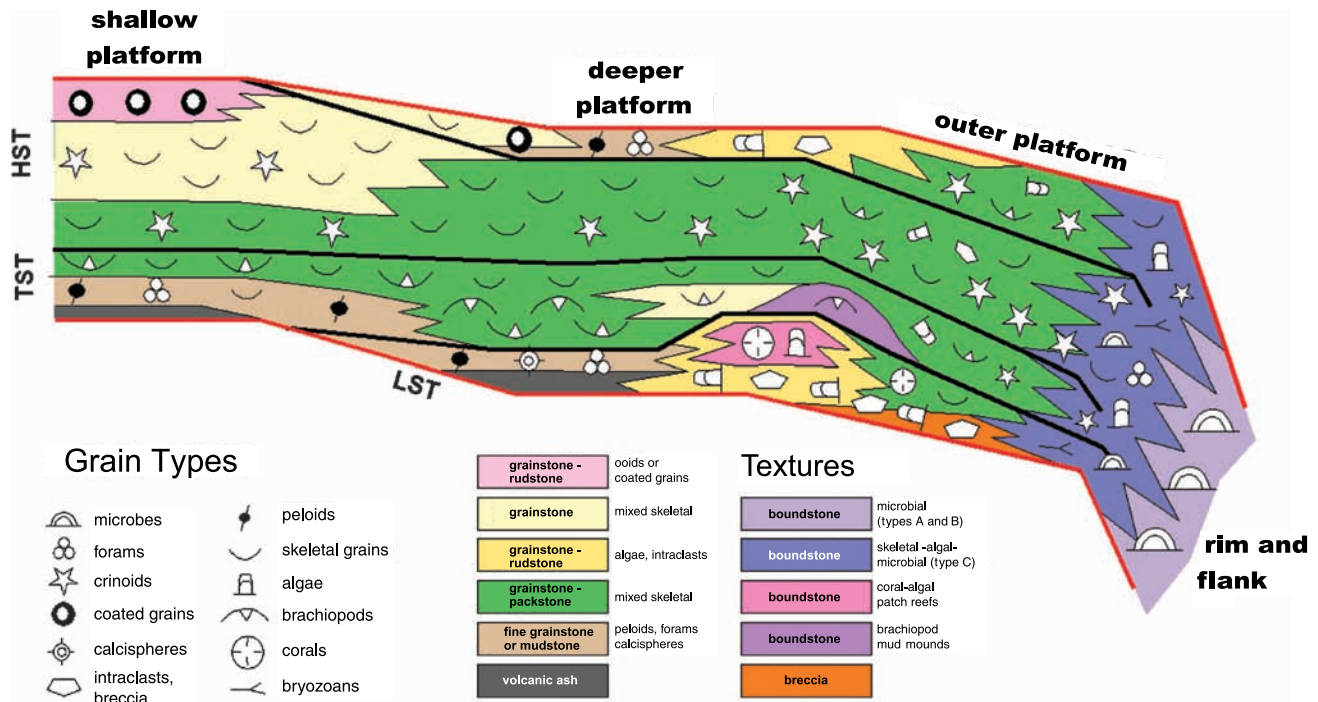


**FIGURE 4.** Idealized Tengiz fourth-order platform sequence, showing textural and compositional variations associated with platform bathymetry for the Bashkirian, Serpukhovian, and late Viséan. Outer-platform, rim, and flank facies illustrated apply particularly to the Serpukhovian. For other intervals, outer-platform facies, in general, are characterized by an increase in algal grains, micritic intraclasts, and coarse crinoid-brachiopod debris. Sea level lowstands are associated with exposure of shallow-platform shoals, contemporaneous formation of an outer margin complex of algal-intraclast grainstones and possible coral-algal patch reefs, and local development of restricted conditions on the platform. Partly restricted-marine conditions that persisted during the early transgression were dominated by brachiopods, including the formation of outer-platform brachiopod mud mounds. Widths of facies belts are not shown to scale.

structural relief<sup>1</sup> (see Figure 2). Evidence for platform compaction includes:

- 1) a lack of volumetrically significant deep lagoonal facies in the central areas of the Viséan A, Serpukhovian, and Bashkirian platforms
- 2) upper Serpukhovian and Bashkirian platform cycles in the raised rim that contain shallow facies similar to age-equivalent cycles in the central platform
- 3) significant grain-to-grain compaction observed in thin sections from the platform facies
- 4) observation of high early cement volumes in the rim and flank facies, indicating early development of mechanical rigidity
- 5) a lateral facies progression in Serpukhovian cycles that deepens basinward from the platform

<sup>1</sup> Weber et al. (2003) estimated that approximately two-thirds of the raised rim relief was caused by differential compaction, and one-third was caused by a bioconstructed margin associated with upper Bashkirian cycles.

into the rim, based on comparisons between Tengiz and other microbial boundstone-cored platforms (Kenter et al., 2005).

The break in slope separating the raised rim and flank areas does not necessarily indicate the limit of Serpukhovian progradation. In some regions, this break appears to be controlled by faulting or mass wasting. In addition, differential compaction of a basinward-thickening wedge of middle- to lower-slope facies may be responsible for the slight basinward dip of the raised rim observed in some areas.

#### *Rim and Flank Depositional Environments*

The rim and flank contain carbonate facies deposited in water depths ranging from a few meters to several hundred meters. Facies descriptions come mainly from cores<sup>2</sup> and from Formation MicroImager (FMI)

<sup>2</sup> Approximately 1200 m [3937 ft] of core from 15 wells available as of year-end 2005 were examined for this study.

logs calibrated to cores. Facies interpretation from FMI logs was hampered by use of oil-based mud during drilling, which tended to reduce conductivity contrasts between porous and nonporous rock, and by frequent hole washouts and zones of lost circulation that adversely affected image quality. Rim and flank facies are associated with a depositional profile consisting of the following environments, in the order of increasing paleowater depth:

- 1) cyclic shallow-platform deposits
- 2) outer-platform skeletal-intraclast rudstone, grainstone, packstone, and minor boundstone
- 3) upper-slope microbial boundstone
- 4) middle slope welded to mosaic boundstone breccia
- 5) lower-slope detrital boundstone breccia and grainy platform-derived deposits
- 6) lower-slope and debris apron boundstone breccias and bedded, fine-grained periplatform deposits.

These are partly based on environments and facies recognized in outcrops of the Asturias platform margin in the Cantabrian region of northern Spain and from the Capitan margin in west Texas and New Mexico (Figure 5). The Tengiz outer platform, slope, and debris apron facies are described in the ensuing paragraphs and are also summarized in Appendix 1. The cyclic, shallow-platform facies are described in Kenter et al. (2006).

### ***Outer-platform Facies***

The Asturias and Capitan margins were both formed by deeper water microbially influenced boundstone margins (Kirkland et al., 1998; Della Porta et al., 2003) and support the interpretation of considerable original outer-platform relief above the Tengiz upper slope during the Serpukhovian. The Asturias margin had outer-platform relief of between 20 and 50 m (66 and 164 ft) during times of progradation (Bahamonde et al., 2000; Kenter et al., 2005). Estimates of the relief across the Capitan outer platform margin show variations through time from 10 m to more than 60 m (33 to more than 197 ft) (Kerans and Harris, 1993; Tinker, 1998). Total paleobathymetric relief from the shallow Tengiz platform to the start of the upper-slope microbial boundstone at the edge of the outer platform was at least tens of meters (Weber et al., 2003) and probably higher. Apparent thickening in the outer platform of the uppermost Serpukhovian fourth-order cycles, plus the limited presence of subaerial exposure at the tops of outer-

platform cycles, indicates that relief exceeded at least some of the ambient low-amplitude eustatic variations, estimated to be between 25 and 50 m (82 and 164 ft) (Ross and Ross, 1987, 1988).

Whereas the succession of facies comprising cycles in the central platform area is well documented in cores (see Kenter et al., 2006), the descriptions of Serpukhovian outer-platform cycles contained here are generalizations based on a limited number of complete cycles present in the current suite of cores. The basal parts of some outer-platform cycles were observed to contain breccias composed of colonial coral detritus or, in other cases, rounded, platform-derived grainstone clasts (Figure 6A, B). The breccias contain either microbial matrix textures and cements or a matrix of coarse skeletal debris. They may represent lowstand deposits, indicating updip platform exposure, or development of outer-margin coral patch reefs. In other sequences, brachiopod mud mounds a few meters thick (Figure 6C) are encountered near the base. The middle and upper parts of cycles are characterized by wackestones, packstones, and rudstones containing large crinoids, brachiopod shell fragments, and solitary rugose corals (Figure 6D), indicating an increase in water depth. This facies is associated with dipping beds (Figure 6E), indicating deposition on a paleoslope, and may also exhibit microbial matrix textures. Cycle tops tend to be characterized by a reduction in crinoid-brachiopod-coral grains and an increase in coated-grain or algal-intraclast grainstone, resembling some shallow-platform grainstones. Subaerial exposure effects like those described from the central platform (Kenter et al., 2006) are commonly absent, but large dissolution voids filled with multilayered geopetal sediment and multiple generations of carbonate cement are found, as are brecciated grainstone intervals with evidence of clast rotation and mixing. Isolated, sediment-filled dissolution voids are also scattered throughout the section, but appear to increase in frequency at or near the tops of cycles. These may be associated with longer term exposure at supersequence boundaries (Serp\_SSB and Bash\_SSB), or they may be unrelated dissolution features whose distribution was influenced by stratigraphic permeability variations.

### ***Upper- to Middle-slope Facies***

The upper slope consists mainly of in-situ microbial boundstone and boundstone breccia. Similar facies are recognized from the Asturias margin (Bahamonde et al., 2000; Della Porta et al., 2003) as mentioned

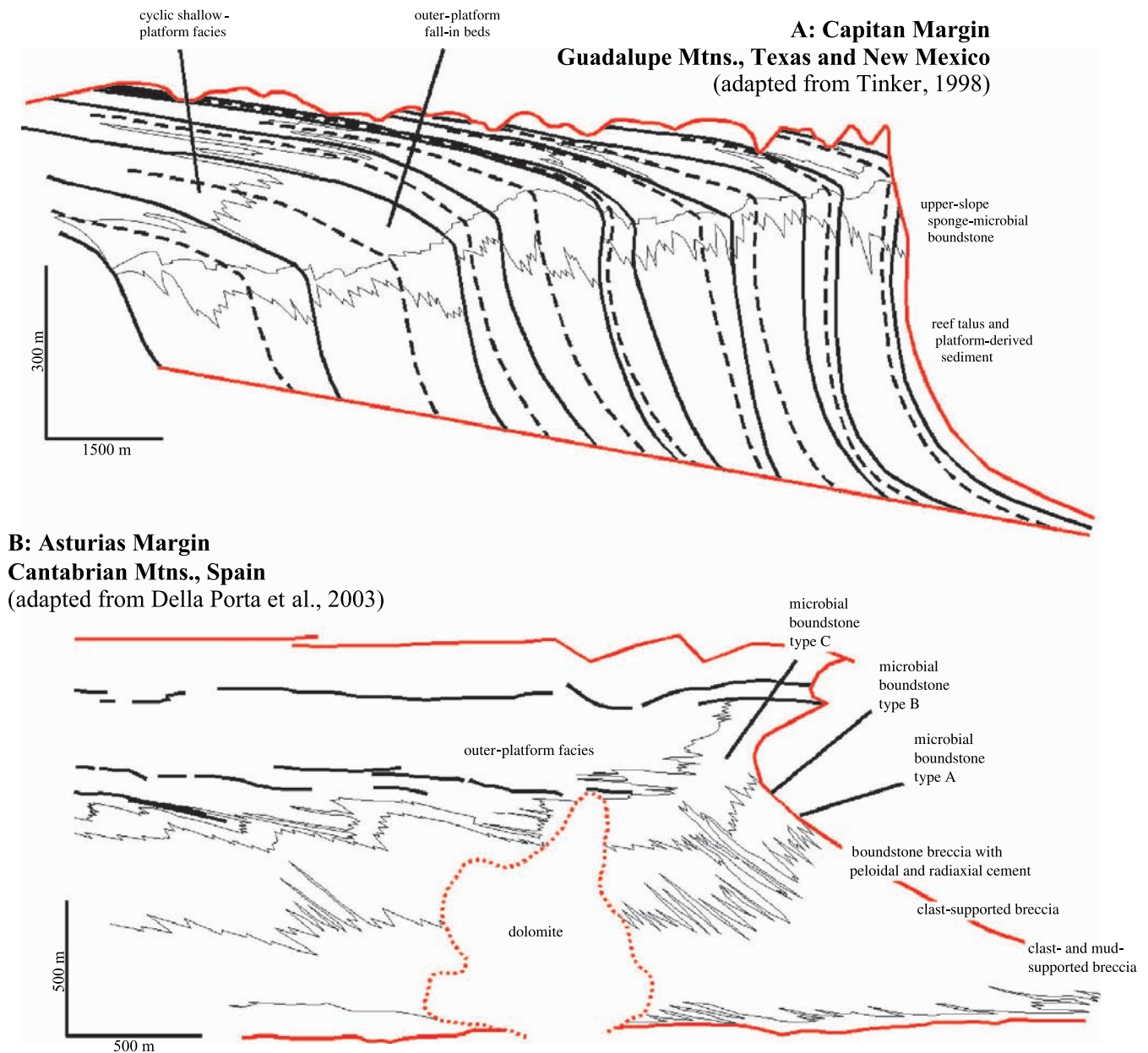


**FIGURE 5.** Outcrop analogs with facies and depositional relationships similar to the Tengiz outer platform, rim, and flank. Like Tengiz, the platform margins illustrated are characterized by dipping, basinward-deepening platform facies that pass downward into upper-slope, microbially influenced boundstones and foreslope facies with reef-derived breccias. Based on these profiles, the structurally raised rim visible on Tengiz seismic data (see Figure 3) is largely an artifact of postdepositional differential compaction (see text for discussion). Microbial boundstone types A, B, and C noted in the Asturias example closely match boundstone types recognized in Tengiz cores.

previously, from Triassic platforms in Italy (Blending, 2001) and from Famennian platforms in the Canning basin (Playford, 1984; Kerans et al., 1986; Stephens and Sumner, 2003). Tengiz cores and FMI logs suggest that the in-situ boundstone interval is perhaps 150–200 m (492–656 ft) thick. In-situ microbial boundstones (Figure 7) are light colored in core, with textures that include relatively featureless

micritic to peloidal fabrics (type A) or irregular laminar fabrics and amalgamated semiconcentric laminar masses (type B). A third boundstone type (type C), characterized by massive to peloidal fabric with common skeletal grains (bryozoans, algae, forams, ostracods, pelecypods, crinoids, corals, and sponges), represents the transition between upper-slope and outer-platform facies. Small- to medium-size fenestrae filled with banded

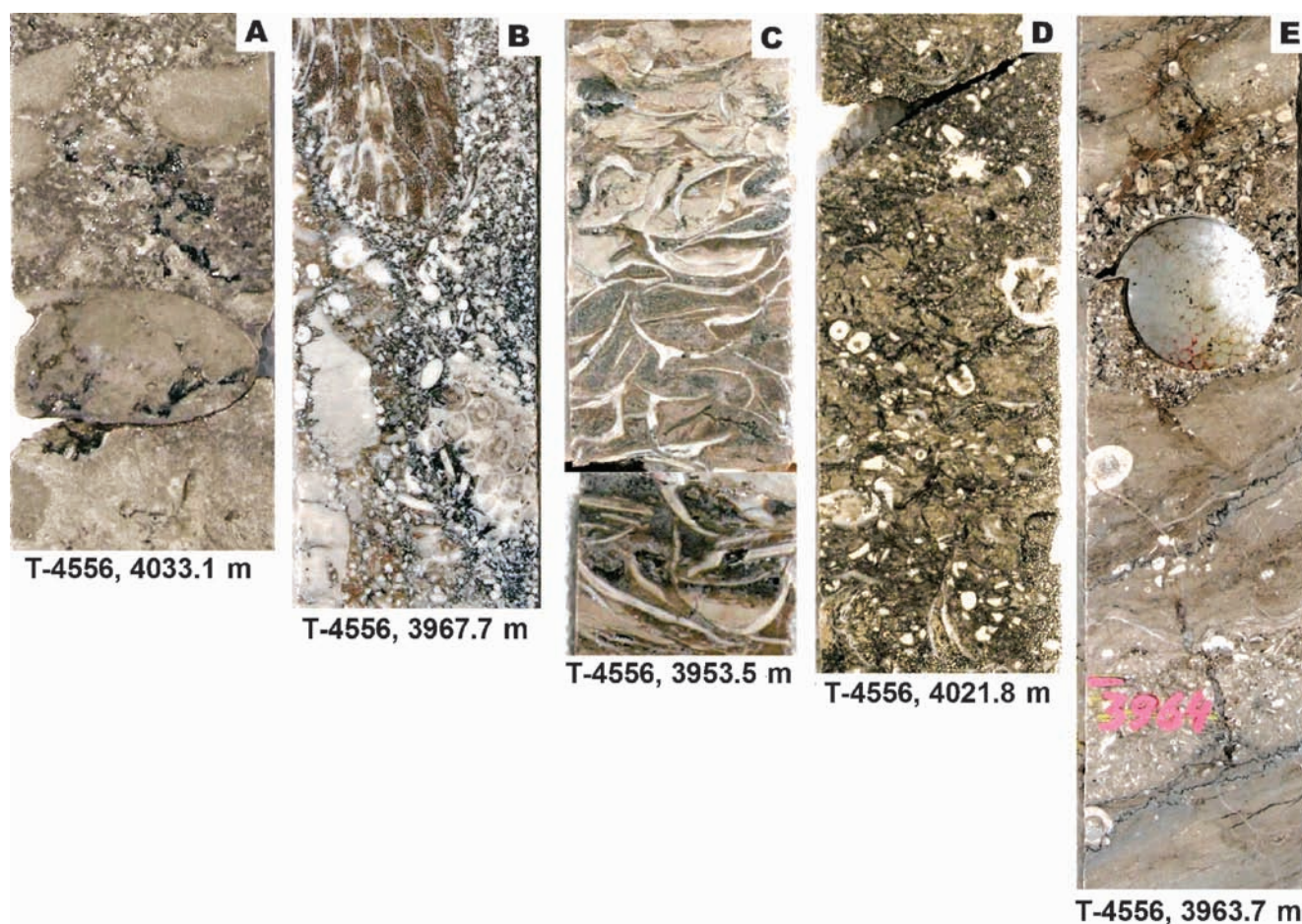


**FIGURE 6.** Serpukhovian outer-platform facies. Breccias composed of platform-derived clasts (A) or colonial coral fragments (B) occur toward cycle bases. The breccia in (A) contains cement and clotted fabric of possible microbial origin, whereas the matrix in (B) consists of coarse crinoidal rudstone. Brachiopod mud-mounds (C) as much as a few meters thick also sometimes occur near cycle bases. The middle and upper parts of typical outer-platform cycles contain abundant packstone and wackestone with large crinoids, brachiopods, and solitary corals (D), as well as intervals with dipping beds (E), indicating deposition on a paleoslope.

cements are commonly abundant, and larger cement-lined cavities filled with internal sediment or skeletal accumulations are observed. Boundaries between microbial masses are sometimes formed by networks of elongate cavities that are also frequently cement filled.

The boundstone interval at Tengiz could be extended down to more than 300 m (984 ft) if certain types of breccias are included. The upper slope interval in the Asturias margin is comparable in thickness and includes both in-situ microbial boundstone, and nearly in-situ boundstone breccia generated by rapid marine cementation of incipient boundstone failure (Bahamonde et al., 2000; Della Porta et al., 2003). To date, similar breccias held together by thick marine cements have not been observed in abundance at Tengiz, although core coverage is still limited. However, breccias consisting of irregularly shaped to

subangular boundstone clasts with stylolitic (welded breccia) or fracture (mosaic breccia) contacts are found in the Tengiz middle to upper slope (Figure 8) and may be analogous to the Asturias intact breccias. The matrix consists mainly of several generations of calcite cement, secondary microbial encrustations, microbial cement, and minor amounts of platform-derived skeletal sediment, thin-bedded marly volcanics, or argillaceous carbonate. Very little open primary pore space was observed in these breccias.

Formation MicroImager logs over upper-slope microbial boundstone and breccia intervals show little evidence of cyclicity, suggesting that sea level variations that affected the platform had little or no effect on production of microbial boundstone. As a result of deposition below the range of sea level fluctuations and productivity across a wide range of water depths,

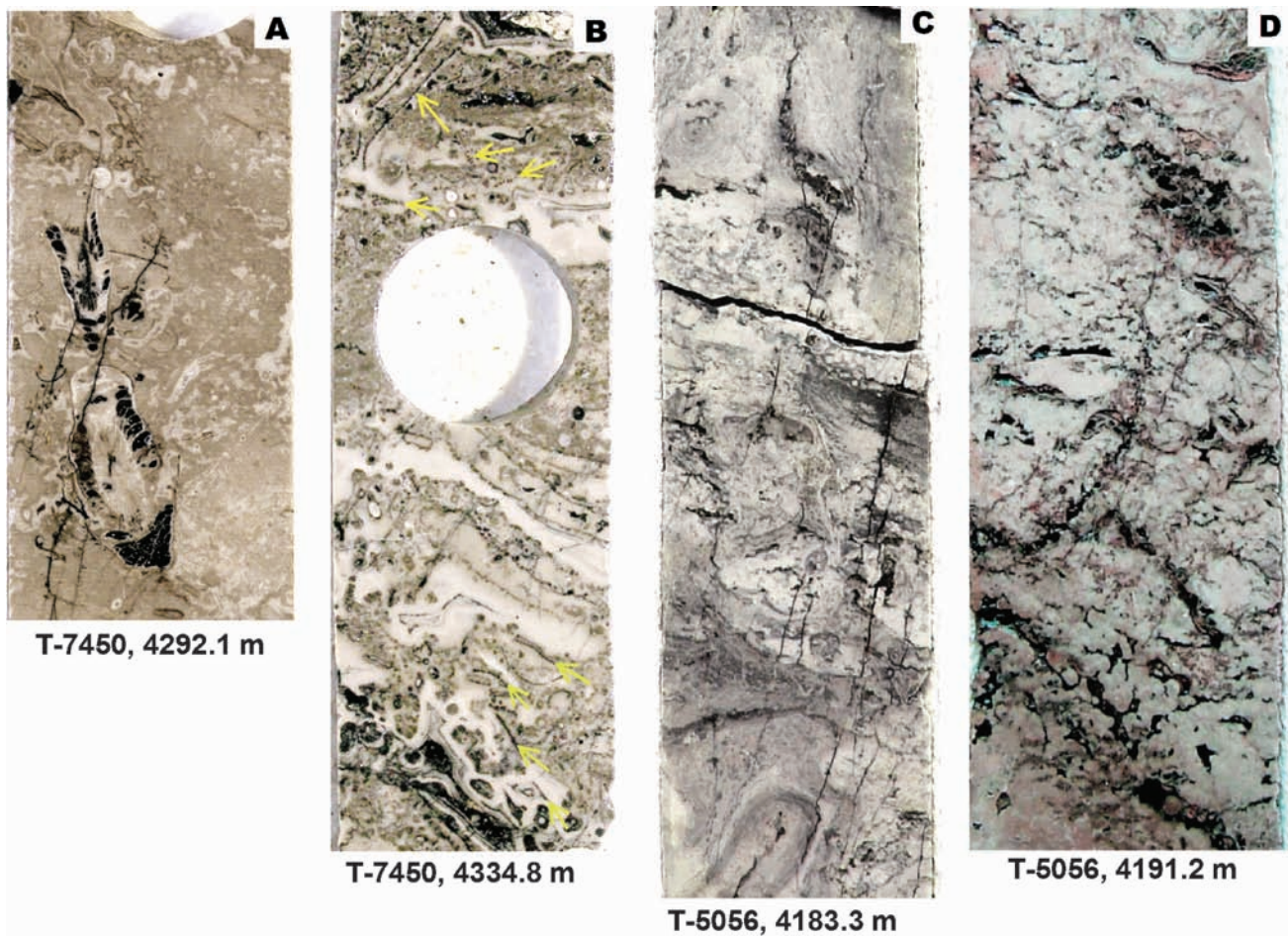


**FIGURE 7.** Serpukhovian microbial boundstone facies, shown in order of increasing paleodepth. (A) Type C boundstone (skeletal-micritic) with corals and crinoids, and numerous cement-filled, irregular-shaped fenestrae. The matrix is skeletal rich with micritic to peloidal microbial texture. (B) Type C boundstone containing numerous bryozoans (arrows) and thick-banded cements of probable marine origin. (C) Type B boundstone (laminar cemented), characterized by irregular to rounded, concentrically laminated microbial masses. These boundstones contain as much as 75% cement. (D) Type A boundstone (peloidal-micritic), featuring a dominantly peloidal to micritic matrix, scarce fauna, and numerous fenestrae or tubular voids.

including subphotic depths, the boundstones were apparently able to prograde continuously seaward during all stages of sea level rise and fall.

#### ***Middle- and Lower-slope Facies***

The middle and lower slope consists of mainly detrital facies (Figure 9), including sedimentary boundstone breccias; coarse skeletal rudstones; fine-grained breccias; massive or poorly bedded allochthonous grainstones; and thin-bedded to laminated grainstones, packstones, wackestones, mudstones, argillaceous carbonates, volcanic ashes, and cherts. Clast size and packing varies in the breccias, with textures ranging from matrix-supported floatbreccia to welded breccia with stylolite-bounded clasts (Figure 9D–F). Clast sizes range from less than 1 cm (0.4 in.) to several meters.

The matrix contains variable amounts of bioclastic debris, fine-grained carbonate, argillaceous mudstone, and volcanic ash. The most visible skeletal components are large crinoids and brachiopod shell fragments similar to outer-platform facies. Relationships between clast size, clast packing, matrix grain size, and matrix composition have not been fully evaluated, but they appear to be poorly correlated. Clasts are dominantly upper-slope microbial boundstone fragments, although platform-derived clasts and reworked slope clasts are increasingly observed in breccias near the base of the section. Some detrital breccias are massive and unbedded over very thick intervals, whereas others are layered and contain intervals of bedded, grainy periplatform facies. Formation MicroImager logs again do not indicate an ordered cyclicity that can be related to the platform sequences.

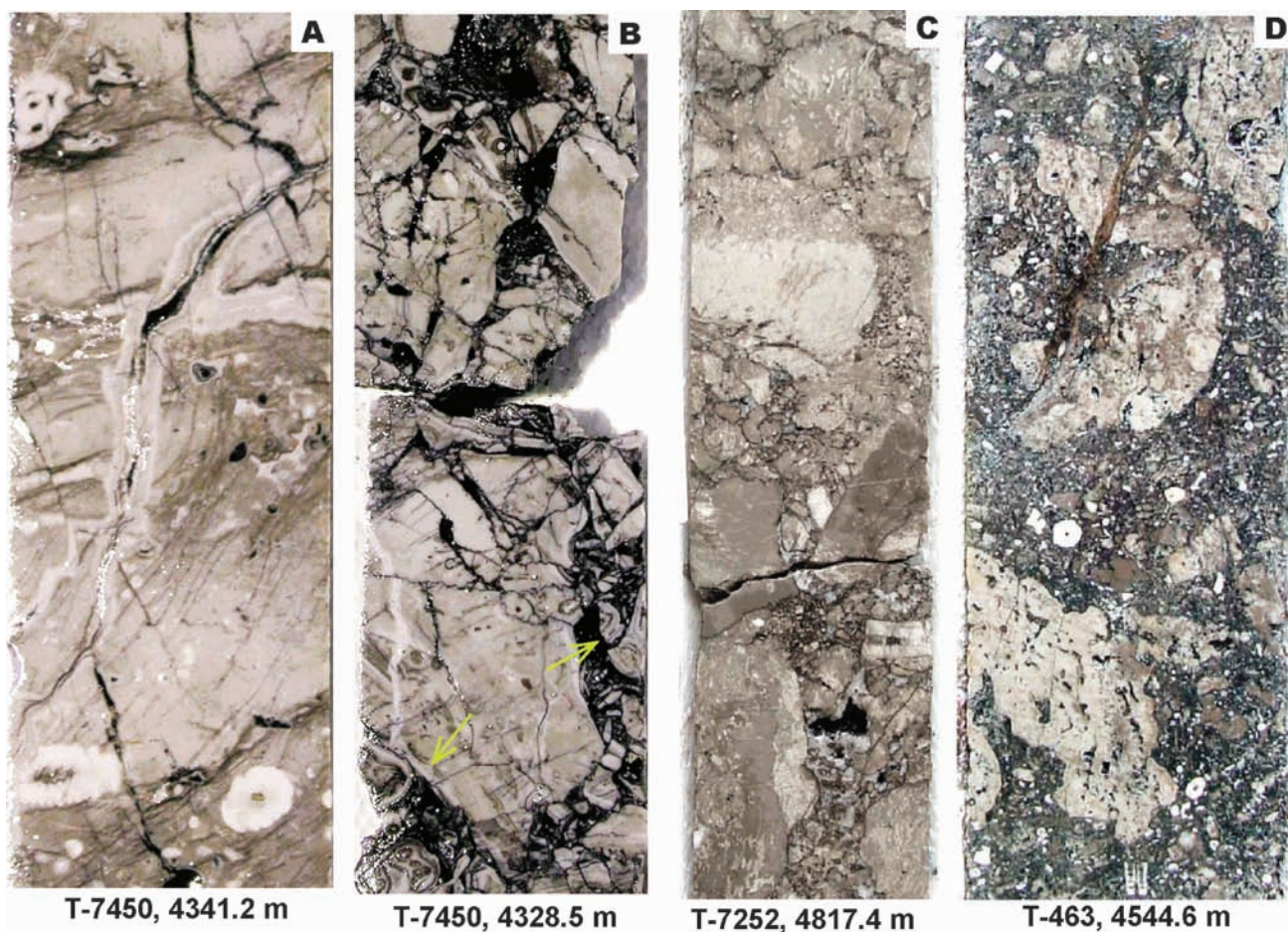


**FIGURE 8.** Upper- to middle-slope diagenetic and sedimentary breccias. (A) Fractured microbial boundstone healed by banded, probably marine cements. (B) Partly cemented mosaic breccia containing earlier cemented voids dissected by later fractures and voids containing bitumen and equant calcite spar (arrows). Larger open voids are mostly a product of leached cement fills in the secondary breccia. Note also that the early, cemented fracture in (A) is also intersected by a later, bitumen-filled fracture. (C) Mosaic to welded breccia containing microbial boundstone clasts with stylolitic contacts. (D) Sedimentary floatbreccia with irregularly shaped boundstone clasts, and crinoid-rich, skeletal-lithoclast rudstone matrix.

### DEPOSITIONAL HISTORY OF THE TENGIZ RIM AND FLANK

The additional facies control provided by FMI logs (Figure 10) proved helpful in interpreting the rim and flank regions. Attempts to extrapolate fourth-order platform correlations into the rim and flank on ordinary wire-line logs proved difficult because of the presence of apparently nonstratiform porosity variations and diagenetic effects manifested as anomalous radiogenic responses on gamma-ray logs. Additionally, rim and flank stratigraphy is complicated by large-scale failure and mass wasting because of instability, both during and after deposition. Seismic and biostratigraphic control indicates that the interval contains breccias of Serpukhovian age as well as Bashkirian-aged breccias with Serpukhovian clasts. Boundstone

breccia is the dominant facies present in rim and flank cores recovered to date; therefore, its distribution is a critical element of reservoir prediction. This requires a deeper understanding of depositional and failure processes at the Tengiz margin.

The analogous Asturias and Capitan platforms are also associated with middle- and lower-slope breccia deposits. The Asturias breccias occupy a basinward-thickening middle- to lower-slope wedge (see Figure 5), whereas the Capitan margin is associated with both middle- and lower-slope breccias and basal debris flows out in front of the shelf (Melim and Scholle, 1995). These dominantly progradational margins have maximum upper-slope angles of 30–35° (Tinker, 1998; Della Porta et al., 2003; Kenter et al., 2005). Slope angles for the Tengiz rim and flank are known from structural and seismic profiles of the Bashkirian

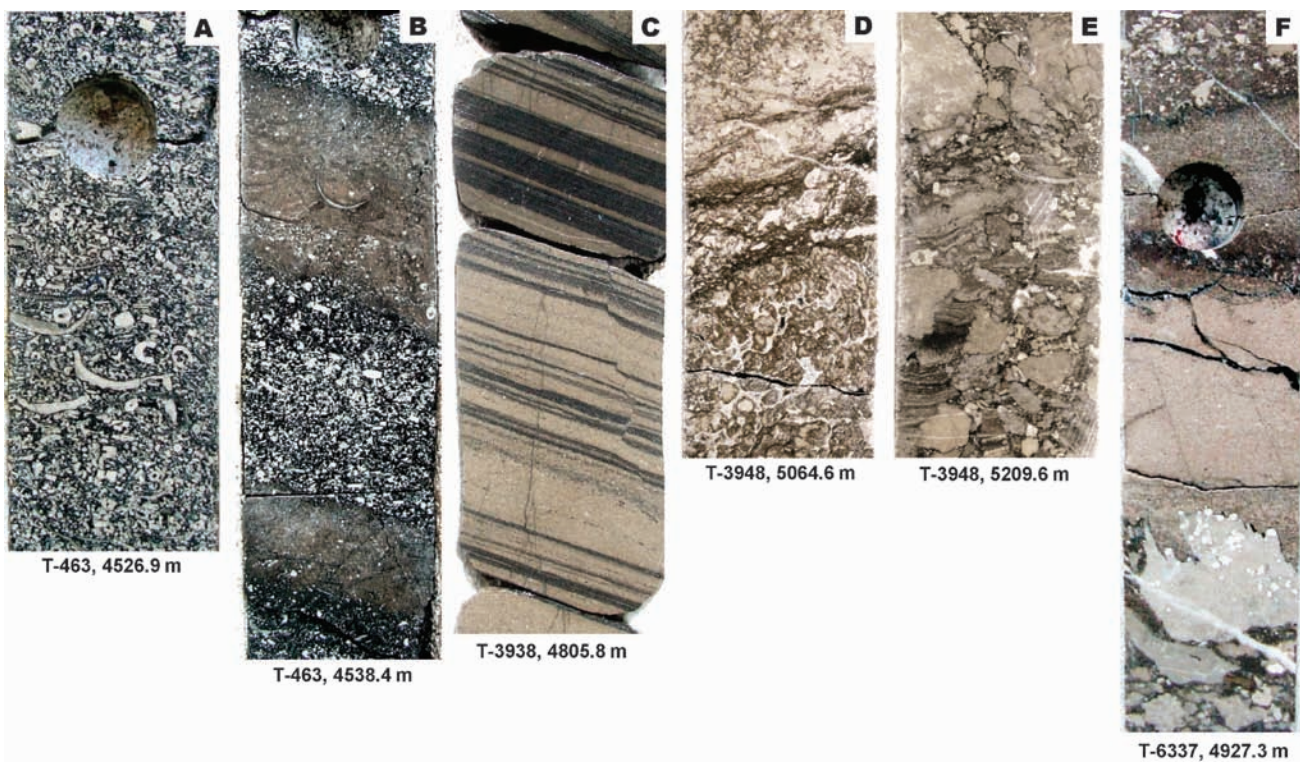


**FIGURE 9.** Middle to lower slope and debris apron facies. Middle- to lower-slope facies include coarse skeletal (crinoid-brachiopod) rudstone (A), skeletal wackestone to packstone with dipping beds (B), and thin-bedded volcanics, mudstone, packstone, and fine grainstone (C). Debris apron facies include coarse breccia with meter-size boundstone clasts (D), packbreccia with platform-derived, crinoid-rich matrix (E), and float- to packbreccia interbedded with allochthonous grainstone and packstone (F). Note the relatively low dip angles in (F).

surface and from dipmeter data. In the steeper sloped upper flank, the Bashkirian is thin, consists of mostly fine-grained deeper water facies, and, thus, forms a prominent seismic reflector that closely approximates the Serpukhovian profile. Measured angles vary between 20 and 25° for apparent accretionary slopes, whereas angles approaching 30° are measured in areas of obvious detachment or failure. These measurements represent angles determined from a compacted body of rock and do not necessarily reflect original depositional dips. Because of the chaotic nature of boundstone and breccia facies at Tengiz, FMI dip measurements commonly produce inconsistent results, but some intervals indicate that preserved bedding dips of 25–30° in the upper slope may be typical, and angles of 35–45° occur locally. Directionality is variable, however, and dips do not always point directly away from the platform. Multiple azimuth changes have been recorded vertically in a single well or in comparing two nearby wells. Formation MicroImager logs also suggest that facies distribution is more complex than expected for simple progradation. Whereas the Asturias and Capitan margin profiles have regular shapes, the Tengiz flank has an irregular shape on

seismic profiles, even considering geometries created by depositional or compactional drape over underlying backstepping platforms. This shape varies systematically around the perimeter of the buildup and, combined with facies obtained from core and FMI logs, allows the rim to be divided into subregions governed by different depositional processes.

#### *Allochthonous and Accretionary Rim Sectors*

The rim and flank area consists of two distinct regions, the allochthonous and accretionary sectors (Figure 11). The allochthonous sector refers to the southwestern and northwestern parts of the rim. It is characterized by a lower, distally thickened apron that onlaps the Tournaisian and Viséan platforms, which itself appears to be downlapped by a narrow progradational wedge (Figure 12A). The raised rim is reduced or, in some places, completely absent along this trend (Figure 12B). The accretionary sector refers to the northern, northeastern, and southeastern regions of the rim, where it is characterized by a conspicuous raised rim crest and a considerably wider progradational wedge (Figure 13A).

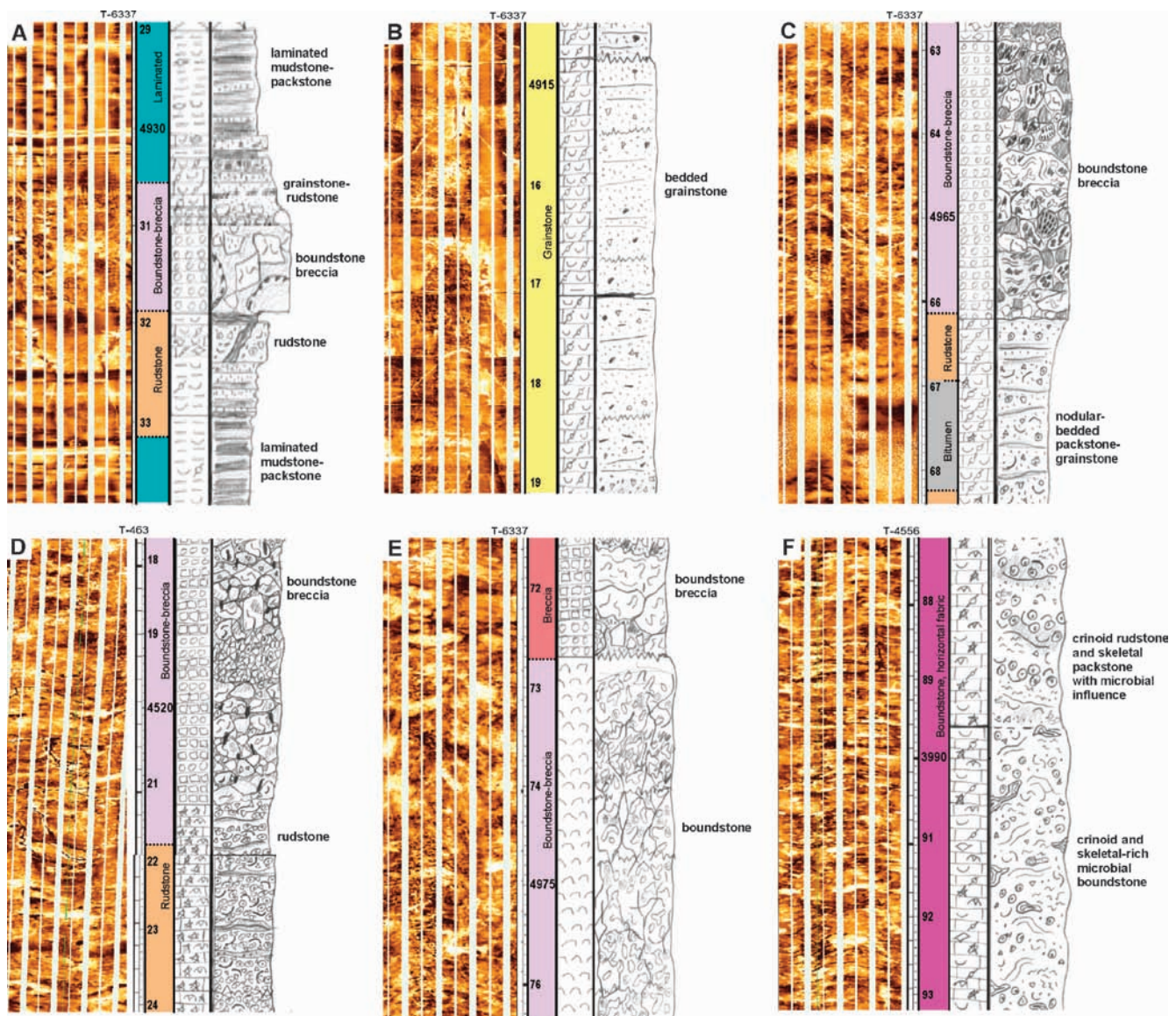


**FIGURE 10.** Formation Microlmager log to core facies calibrations. FMI facies, indicated by different colors in the depth columns (depths are in meters), include boundstone-breccia (BBr), boundstone-horizontal fabric (Bhz), breccia, rudstone, grainstone, and laminated fine-grained (lam-FG). BBr facies, characterized by a chaotic image lacking horizontal layering (C–E), includes both boundstones and breccias from core, which, except occasionally, were not distinguishable on FMI logs. Bhz facies corresponds to poorly bedded outer platform skeletal rudstone and type C microbial boundstone (F). FMI rudstone is characterized by nodular texture and some horizontal layering (A, D) and includes lithoclast-skeletal rudstones, fine-grained breccias, and poorly bedded skeletal packstone, wackestone, and floatstone from core. Formation Microlmager grainstones, identified by a low-contrast image with faint layering (B), correspond to generally tightly cemented allochthonous grainstones. Lam-FG facies, marked by frequent high-contrast layers (A), are equivalent to thin-bedded, deep-water volcanics, mudstones, and grainstones in core. In some intervals, image quality is adversely affected by bitumen, which produces a snowy texture overprinted on the facies (C).

In the allochthonous sector, the lower apron consists of bedded to massive boundstone breccia interlayered with bedded platform-derived sediments, suggesting relatively continuous failure of a boundstone margin. In the northern half of the accretionary sector, the flank slope is typically irregular. This is partly caused by a series of local slump scars and ap-

parently bottomless faults, but also to a prominent mid-slope bulge. The lateral continuity of this latter feature (see Figure 11) could be accounted for by slight downslope movement of upper-slope material or alternately by downlap of a late-stage progradational wedge onto a protruding debris apron (Figure 13B), analogous to the allochthonous sector. Seismic data

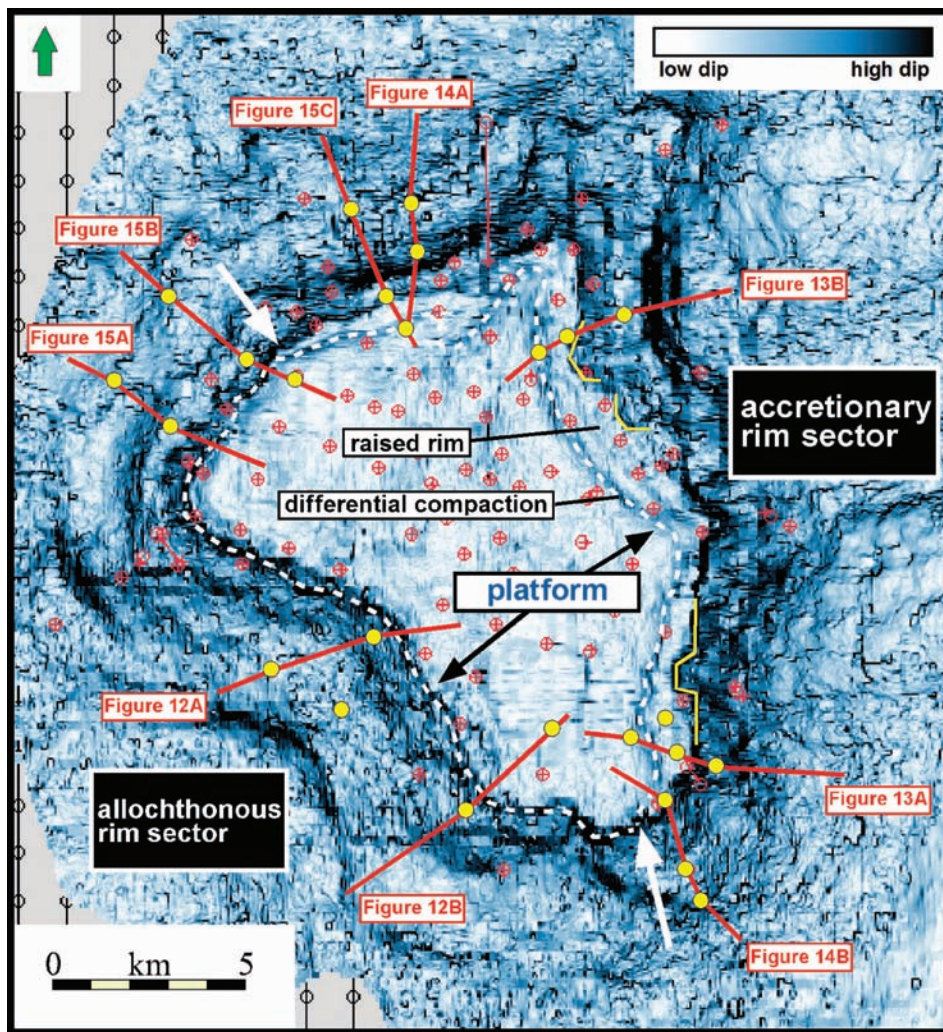


**FIGURE 11.** Dip magnitude on the top of the reservoir (Bashkirian surface) measured from 3-D seismic data, showing the extent of the accretionary and allochthonous sectors. The map shows a thin band of elevated dip (dashed white line) that is directed toward the platform interior caused by differential compaction between platform facies and upper-slope microbial boundstones and indicates the position of the platform margin prior to progradation. The zone of low dip between this band and the slope break is the raised rim and indicates the limit of progradation (possibly modified by failure processes). The boundary between the accretionary and allochthonous sectors occurs where the band of compactional dip intersects the slope break (white arrows). In the accretionary sector, the slope break is marked by several local scarps indicative of localized failure (yellow lines). In the allochthonous sector, the raised rim is thin or absent, indicating either nearly complete rim failure or a poorly developed progradational wedge. The locations of seismic profiles in Figures 12–15 are also shown.

suggest the existence of an early debris apron in the accretionary sector in another way as well. The northern and southern margins of the Tengiz platform represent transitional regions between the allochthonous and accretionary sectors. Both areas are characterized by an upper wedge that gradually widens eastward while maintaining a downlapping relationship to laterally continuous debris apron deposits (Figure 14).

The accretionary and allochthonous sectors demonstrate internal and comparative differences with respect to the total volume of rock in the rim and flank, as well as the relative proportions in the upper wedge and lower apron. This asymmetry could result from both extrinsic and intrinsic controls. For example, one intrinsic control might be the pre-Serpukhovian profile created by the stacking pattern of Tournaisian and Visean platforms. In areas of significant backstepping, a bench or gentle slope might have provided stability for progradation (see Figure 13A), whereas in areas where platform stacking is more vertical, instability and rim failure might dominate. Alternatively,

primary microbial production may have varied around the platform. In the accretionary sector, elevated productivity could have resulted in faster accumulation of a debris apron and, thus, earlier initiation of upper wedge progradation. In a lower productivity allochthonous sector, the debris apron required a longer time to accumulate and was perhaps still in progress at the end of the Serpukhovian, accounting for the more limited upper wedge development.

Tectonic activity is a possible external mechanism that could also account for rim asymmetry. Rim failure could have been restricted to, or enhanced in the allochthonous sector because of alignment with regional stress regimes or as a result of directly facing pressure waves from the tectonically active southern margin of the Precaspian Basin (see Figure 1). Whether the apron is mostly an early or a late feature is therefore still somewhat uncertain because of these possibilities. The significant role of rim failure and the timing uncertainty precluded erecting a stratigraphic framework in the rim and flank that can be specifically

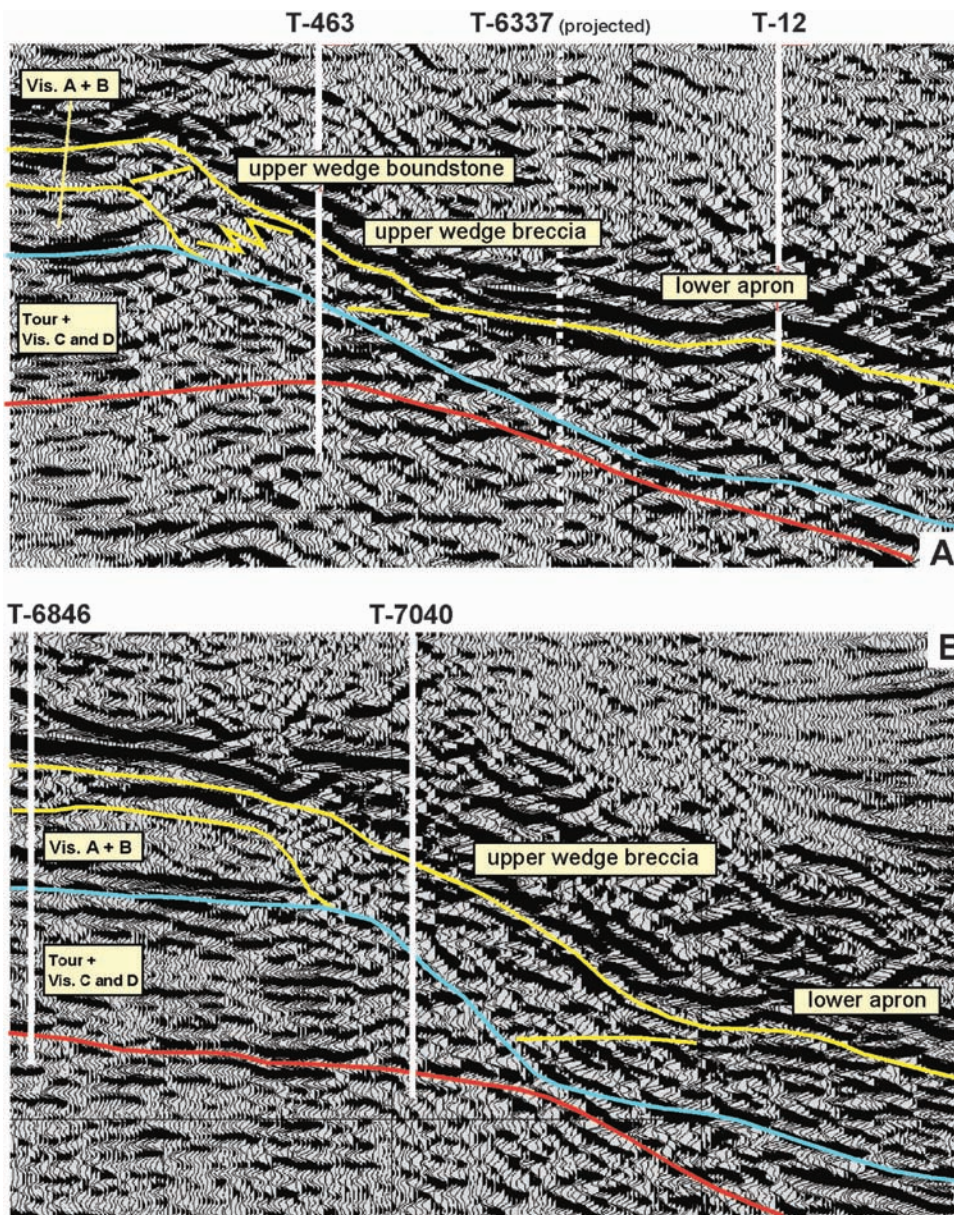


**FIGURE 12.** Seismic profiles from the allochthonous rim sector. In (A), a slightly raised rim indicates a narrow progradational wedge of upper-slope microbial boundstone that formed after deposition of an extensive debris apron. The figure in (B) shows a region where the raised rim is absent, indicating failed progradation. Formation Micro-Imager logs from T-7040 indicate the upper wedge deposits at this location most likely consist of coarse breccia. See Figure 11 for profile locations.

tied to Serpukhovian and Bashkirian fourth-order platform cyclicity; however, core control, FMI facies, biostratigraphic data, and, to a lesser extent, wire-line logs were still used to separately constrain the distribution of facies in the lower apron and the upper wedge as a result of their relative spatial separation.

#### *Upper Wedge Facies Distribution*

From previous discussions, the raised rim effect is interpreted to indicate the presence of mechanically rigid upper-slope microbial boundstone facies in the upper wedge. In places along the allochthonous sector, the upper wedge is partly or completely detached from the platform, and the raised rim effect is absent. In some cases, the wedge appears to have detached more or less intact, whereas in others, it

forms a mound-shaped pile that is almost continuous with the distal apron (Figure 15). To date, the upper wedge is penetrated by 14 wells with core slabs and/or FMI images (T-463, T-4346, T-4635, T-70, T-7040, T-5056, T-5857, T-7252, T-6457, T-4556, T-5059, T-5454, T-7450, and T-7052). These wells indicate facies consistent with a prograding boundstone-cored wedge in areas of accretion in both sectors and facies dominated by breccia in areas of detachment in the allochthonous sector (Figure 16). Specific cored examples include cyclic shallow platform overlying deeper water outer-platform facies (T-4556 and T-7052); upper-slope in-situ boundstone facies (T-7450 and T-5056); and upper-slope boundstone and welded-to-mosaic breccia from a detached but relatively intact upper wedge (T-4635, Figure 15A). Other cored examples include middle-slope breccias (T-5056, T-5857, and T-7252), and middle- to lower-slope clast- and matrix-supported boundstone breccia interbedded with platform-derived crinoid-brachiopod rudstone to packstone (T-463). The Bashkirian in the upper wedge consists of shallow-platform facies in the raised rim area and, on the basis of mainly short cores and core chips from older wells, deeper water facies composed of laminated to thin-bedded mudstones, packstones, fine grainstones, and volcanics in the flank.

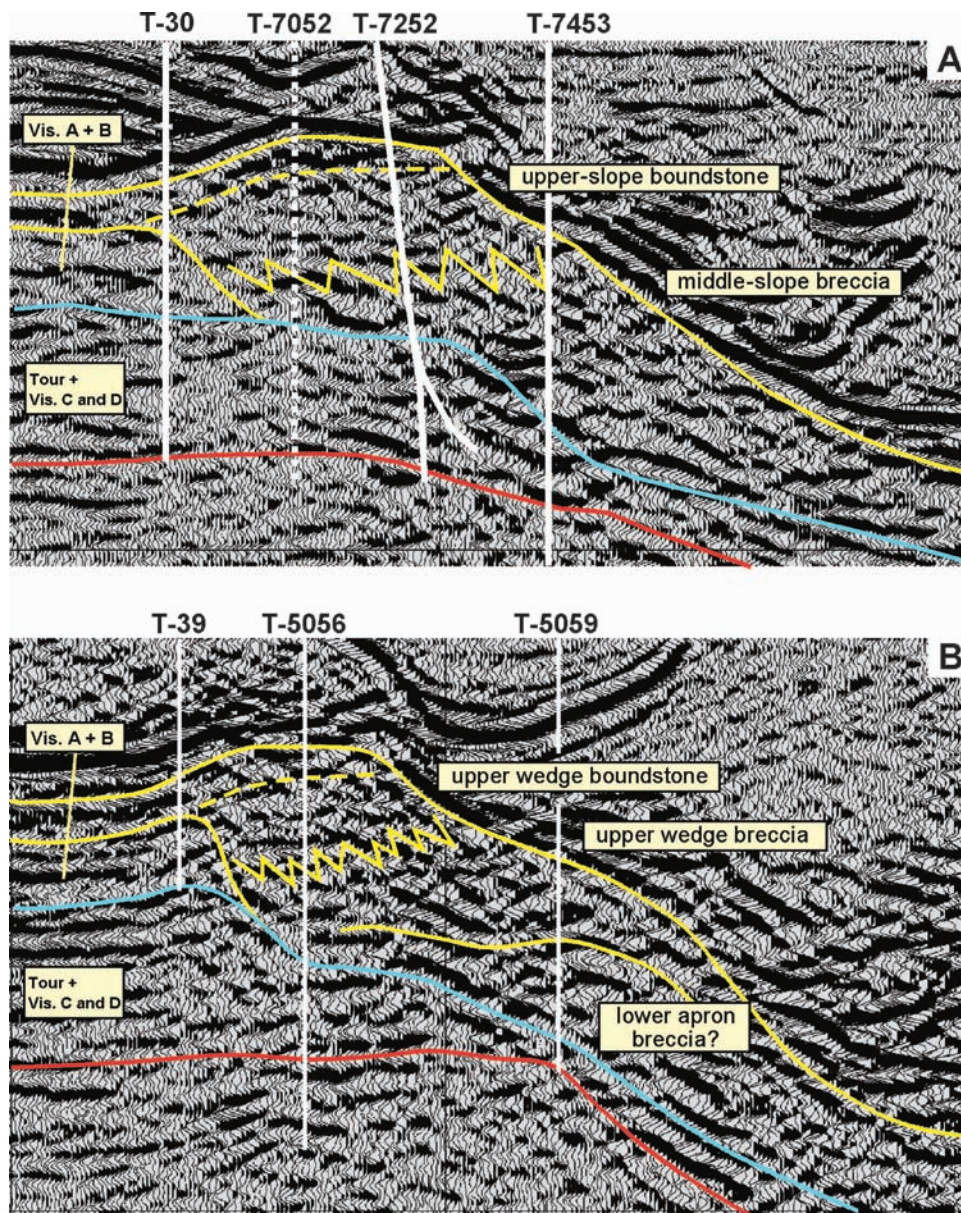


**FIGURE 13.** Seismic profiles from the accretionary rim sector. The flank profile in (A) is smooth and lacks high-amplitude internal reflections. Here, a bench formed by a backstepping of the Visean A and B platforms may have provided stability for early upper wedge progradation. The flank profile in (B) shows a distinct midslope bulge. Formation Microlmager data from T-5059 and T-5660 demonstrate that the upper part of the Serpukhovian interval in the bulge contains a prograding boundstone sequence, whereas the lower part contains bedded boundstone breccias (see Figure 17). The change occurs near a zone of high-amplitude, subparallel reflectors on the seismic line, which have been interpreted to indicate areas in the accretionary sector where deposition of early debris aprons filled in some of the accommodation space as a prerequisite to upper wedge progradation. See Figure 11 for profile locations.

### Lower Apron Facies Distribution

The lower apron is penetrated by four wells in the allochthonous sector with cores and/or FMI data (T-16, T-6337, T-3938, and T-3948). Assuming that an early apron is also present in the accretionary sector, five other wells potentially have representative core and/or FMI data (T-47, T-5963, T-5059, T-5660, and T-6261). In particular, the FMI facies from T-5660 and T-5059, combined with three separate cored intervals from nearby T-5056 in the raised rim, indicate a possible distinction between apron breccias and upper wedge facies in the accretionary sector (Figure 17).

Apron facies are best known from cores in the allochthonous sector, which reveal that, in general, the apron consists of mixtures of upper-slope-derived

boundstone breccia and platform-derived grainy facies, but which also indicate significant lateral variations in bed thickness, clast size, and amount of platform-derived grainy material versus breccia. In two separate cored intervals from T-6337, for example, both clast- and matrix-supported breccias are frequently interbedded with fine-grained periplatform mudstone, packstone, and grainstone. Overall clast size is larger compared to the T-463 core from the upper wedge, but the platform-derived fraction is finer grained. By contrast, a long, cored interval at the T-3948 core consists almost entirely of poorly bedded boundstone breccia made up of very large clasts, with very few interbeds of fine-grained platform-derived material. The T-3938 FMI log suggests that the apron interval there also consists of massive boundstone breccia with few interbeds of platform-derived facies. The lateral extent of this massive, coarser apron breccia facies appears to coincide

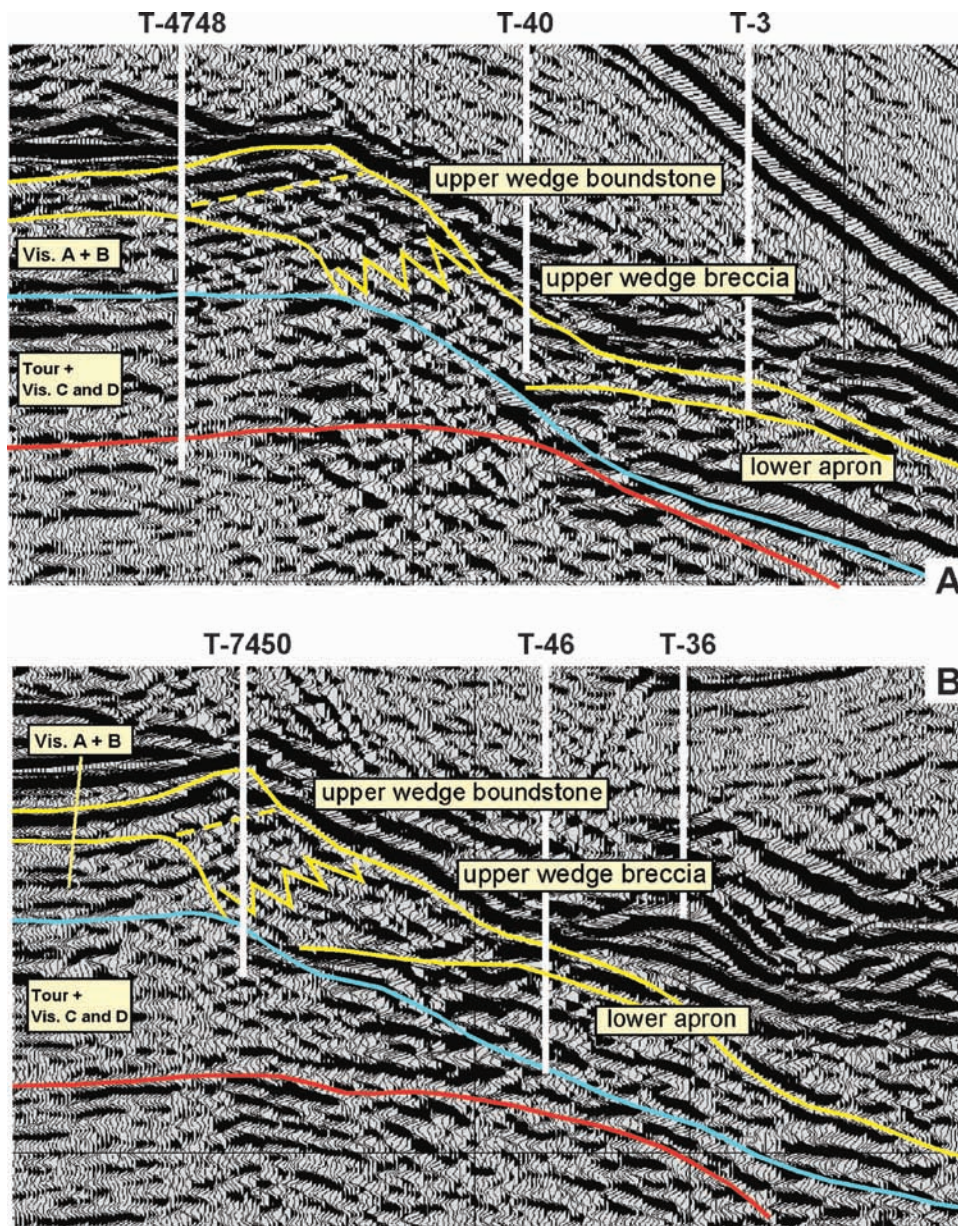


**FIGURE 14.** Seismic profiles from the northern (A) and southern (B) rim and flank regions. These areas are transitional between the allochthonous and accretionary sectors and show both a lower debris apron and significant upper wedge progradation, suggesting that variations in wedge development did not necessarily occur at the expense of the apron. See Figure 11 for profile locations.

sent there. Cores across the base of rim and flank breccias have been recovered at T-6337, T-3938, T-3948, and T-7252. Formation Micro-Imager logs from these and other wells demonstrate that the breccias were deposited abruptly on top of a continuous interval containing mainly thin, dipping beds of deeper water facies. Biostratigraphic analyses from the cores indicate that in both sectors, the onset of breccia deposition occurred close to the Viséan–Serpukhovian boundary.

Biostratigraphic data also demonstrate that Bashkirian-aged sediments containing Serpukhovian boundstone clasts occupy as much as 300 m (984 ft) at the top of

with chaotic seismic character and, therefore, may be regionally mappable within limits imposed by image quality (see Figure 16).

Apron breccias in the allochthonous sector contain increasing numbers of transported slope and platform clasts toward the base of the interval. Cores from T-3938 and T-3948 demonstrate that somewhat finer grained breccias with abundant platform and slope clasts are associated with a resistivity decrease on petrophysical logs. This low-resistivity zone is not observed on logs from the accretionary sector, but because this could be caused by a change in porosity or other diagenetic effect, its absence does not necessarily indicate that similar breccias are not pre-

the apron breccias in the allochthonous sector, indicating that significant postdepositional rim failure occurred in that region. The Bashkirian interval appears to be associated with a distinctive pattern on gamma-ray and resistivity logs (Figure 18), and well correlations suggest that Bashkirian breccias are variable in thickness but laterally extensive (see Figure 16). The apparent absence of equally thick Bashkirian deposits or Bashkirian-aged breccias in the accretionary sector is an important distinction that perhaps indicates that relative depositional stability was achieved in this region prior to the end of the Serpukhovian. Cross sections illustrating the depositional concepts, core and FMI facies control, and typical porosity and

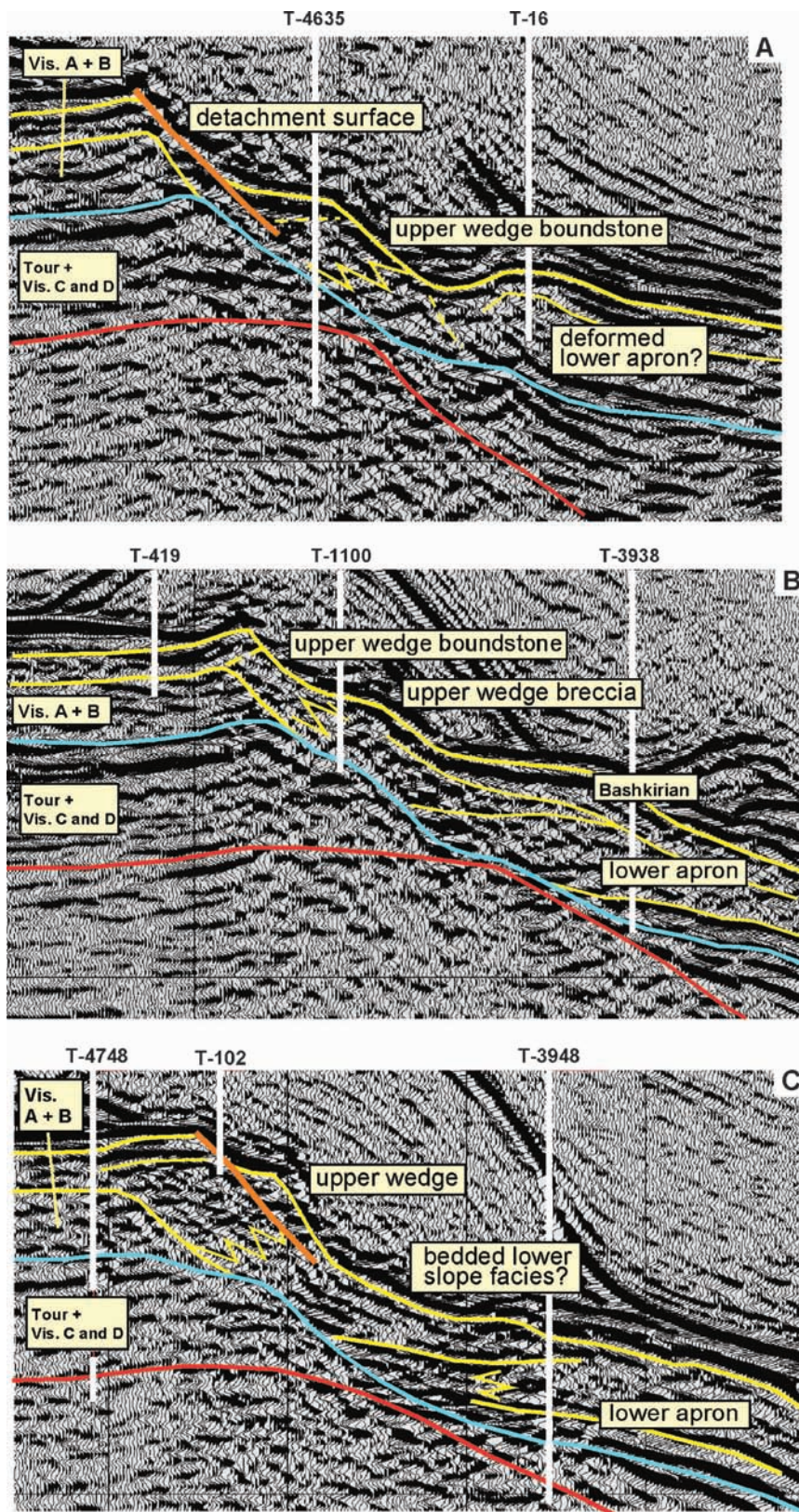


**FIGURE 15.** Seismic profiles illustrating different modes of upper wedge failure. The figure in (A) shows a completely detached but largely intact upper wedge. Core from T-4635 contains mainly type C boundstones and breccias, indicating original deposition in shallower water. The figure in (B) shows a narrow upper wedge with a downslope bulge, indicating possible partial failure. The debris apron in this area consists of poorly bedded boundstone breccia, as indicated on FMI logs from T-3938. Biostratigraphy from drill cuttings revealed a thick Bashkirian-aged section at the top of the apron breccias. The figure in (C) shows local fault detachment in the upper wedge. In addition, chaotic seismic character in the debris apron is separated from the upper wedge slope by a zone of relatively continuous dipping reflections from a distinct lower slope facies. T-3948 cores reveal that the apron at this location consists of massive boundstone breccia with very large clasts. See Figure 11 for profile locations.

## DIAGENESIS

As a long-lived shallow platform, Tengiz was expected to have a complex distribution of pore types because of its multifaceted stratigraphic hierarchy and associated facies variations, repeated exposures to marine, meteoric, and shallow burial diagenesis, and, because of the age range involved, the influences of both greenhouse and icehouse global themes. Core and thin-section observations, combined with preliminary geochemical analyses, provide insights into processes of porosity creation, destruction, and preservation in outer platform, rim, and flank reservoirs and also illuminate relationships that determine reservoir-quality distribution in the rim and flank. These relationships suggest that present-day reservoir-quality variations

are strongly influenced by a late diagenetic overprint involving fracturing, dissolution, and bitumen cementation.

gamma-ray expression of the lower apron and upper wedge in the Tengiz allochthonous and accretionary rim sectors are provided in Figures 18 and 19.

are strongly influenced by a late diagenetic overprint involving fracturing, dissolution, and bitumen cementation.

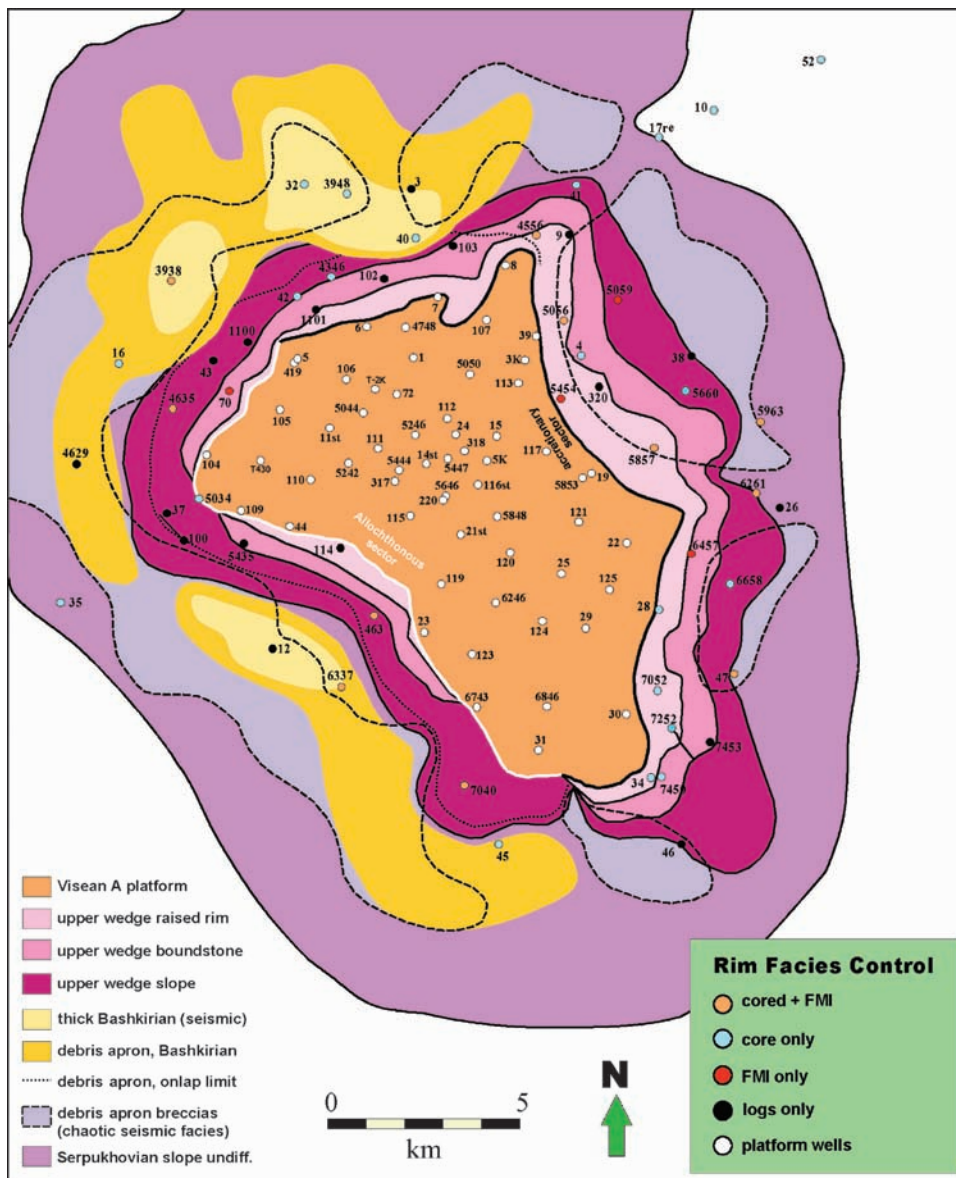


**FIGURE 16.** Facies distribution in the rim and flank. The Visean A outline indicates the platform configuration just prior to Serpukhovian progradation. The raised rim area (upper wedge) represents the preserved extent of Serpukhovian platform progradation. The outer limit of the upper-slope boundstone was determined by an assumed vertical thickness of about 200 m (656 ft) below the slope break. The lower apron contains Serpukhovian and Bashkirian coarse breccias, mapped from seismic character and well-log correlations. Serpukhovian breccias occur on both sides of the platform, whereas Bashkirian apron deposits are generally restricted to the allochthonous sector, indicating depositional instability in that area throughout the Serpukhovian and Bashkirian. Facies control is indicated for rim and flank wells only.

### Early Dissolution, Cementation, and Bitumen Formation

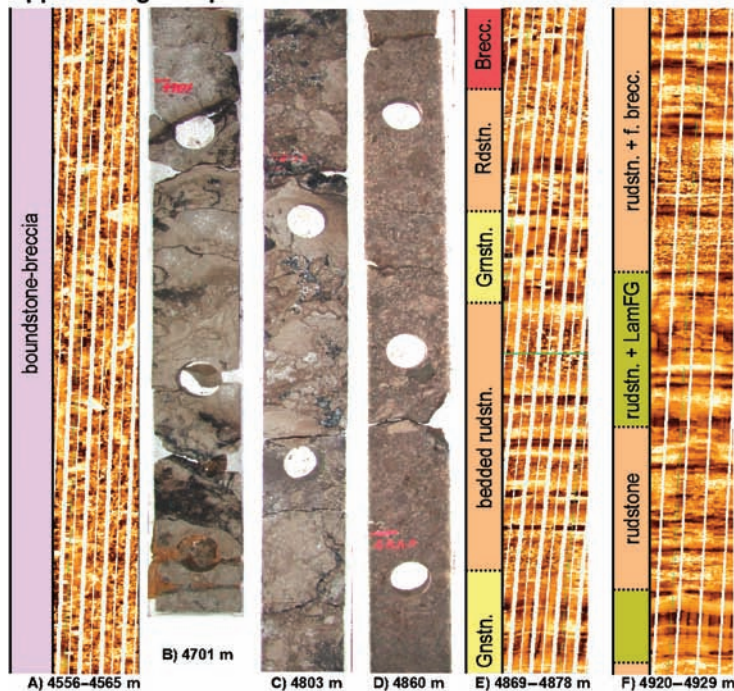
Early pore types consist of primary and early diagenetic matrix pores and larger voids from at least one significant dissolution event. Existing cores suggest that this early dissolution was more prevalent in the outer-platform and upper-slope facies compared to the middle and lower slope. Early dissolution may have occurred during platform margin karst events associated with major sequence boundaries or as a result of Kohout-type convection driven by large fluid-density contrasts between platform-top groundwaters and seawater (Kohout et al., 1977; Saller, 1984; Sanford et al., 1998). Such contrasts, controlled by temperature and salinity, could be especially impor-

tant for platforms like Tengiz with considerable vertical height.

Early voids commonly contain several cement generations. These cements, starting with inclusion-rich calcites of probable marine origin and culminating with medium-

to coarse-grained clear equant calcite of burial origin, form a sequence that destroyed much of the early porosity (Figure 20). The residual pore space commonly contains bitumen, either as a final fill phase or as beads and partial linings on the equant calcite. The early cement sequence is therefore referred to collectively as the prebitumen sequence. Petrographic relationships between bitumen and equant calcite (Figure 20C) suggest that they were emplaced approximately contemporaneously. Equant calcite and bitumen occur in some dissolution features as the only phases, indicating a second fracturing and dissolution event prior to bitumen emplacement. Fluid-inclusion homogenization temperatures indicate that the equant calcite was precipitated at temperatures in the 80–95°C

Upper Wedge Sequence



Apron Sequence

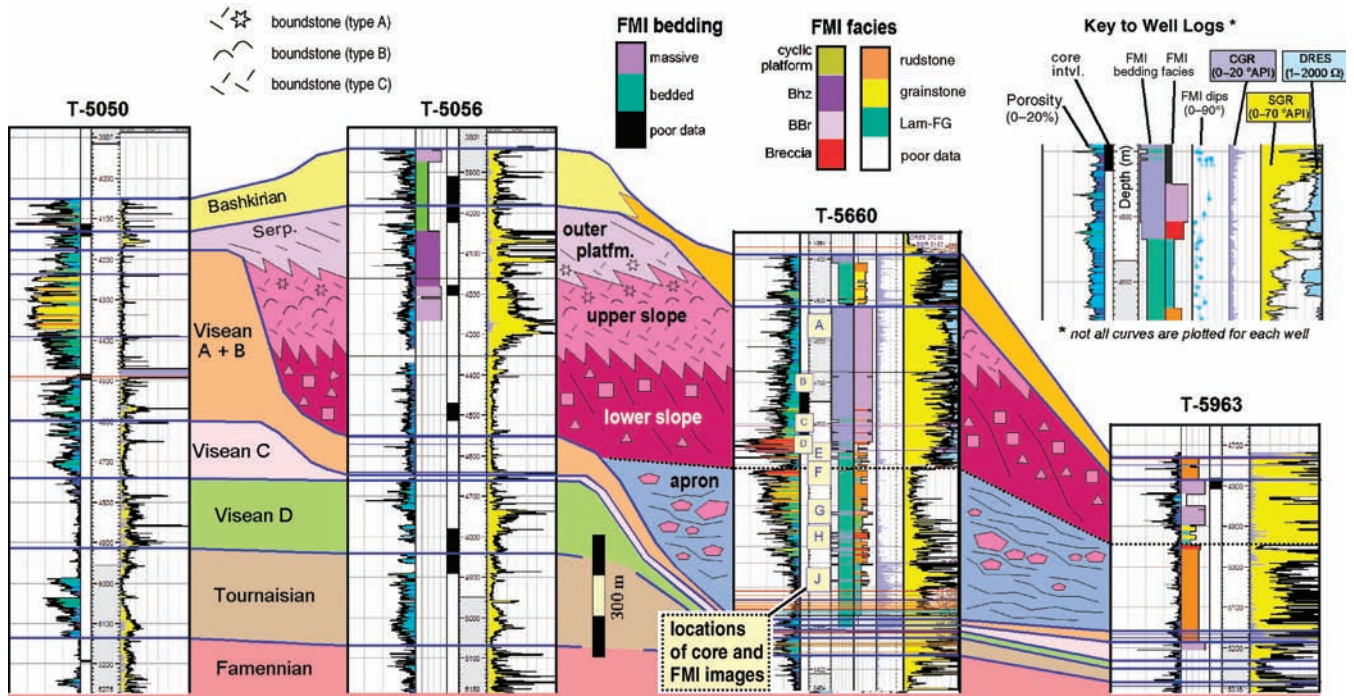
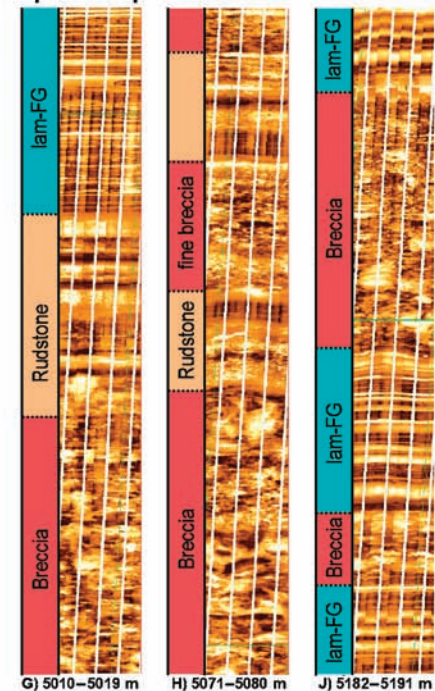
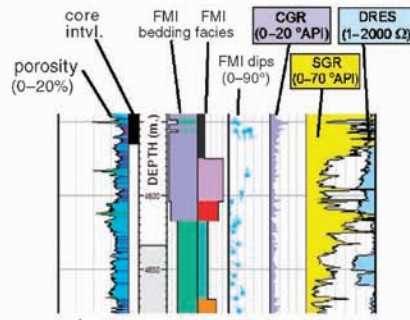


**FIGURE 17.** Selected core and FMI images from T-5660 (top), showing facies representing the upper wedge sequence overlying a possible debris apron sequence in the accretionary sector. The upper wedge sequence consists of distal bedded rudstone and fine breccia toward the base (E, F), which are overlain by successively coarser breccias (B–D). Above the cored interval, the section consists of massive boundstone or breccia (A). The apron (G–J) consists of interbedded lam-FG, rudstone, and breccia FMI facies (the latter presumably containing microbial boundstone clasts). For definitions of FMI facies, see Figure 10. The cross section (bottom, see Figure 16 for well locations) shows that the inferred apron section in T-5660 is associated with reduced radioactivity on the spectral gamma-ray (SGR) log compared to the wedge interval and may be correlated to nearby wells on this basis. Other log curves shown include computed gamma-ray (CGR, calculated with uranium subtracted) and deep resistivity (DRES).

### Rim and Flank Facies

- Bashkirian shallow platform
- Bashkirian deep water + breccia
- Serpukhovian platform
- upper-slope microbial boundstone
- upper wedge breccia
- lower apron breccias and platform-derived facies
- lower apron and platform-derived breccias

### Key to Well Logs \*



\* not all curves are plotted for each well

### FMI facies

- cyclic platform
- Bhz
- BBr
- Breccia
- rudstone
- grainstone
- Lam-FG
- poor data

### FMI bedding

- massive
- bedded
- poor data

### Platform

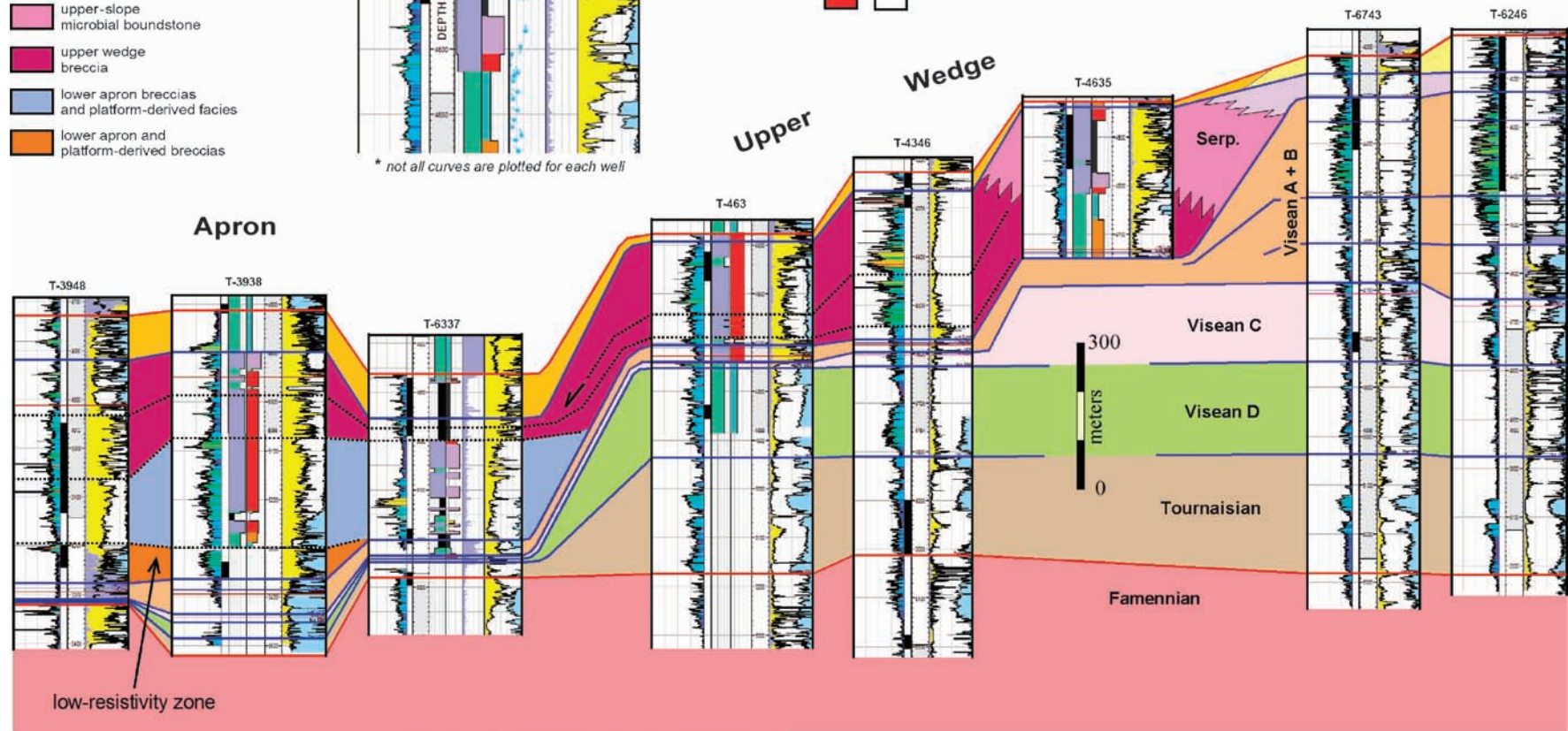


**FIGURE 18.** Facies and stratigraphic relationships in the allochthonous rim sector. Wells are shown in approximate order of increasing distance from the edge of the platform (see Figure 16 for well locations). The thick, allochthonous Bashkirian section at T-6337 is supported by biostratigraphic analysis of the cored interval. Comparison of spectral gamma-ray (SGR) and computed gamma-ray (CGR, calculated with uranium subtracted) logs indicates uranium enrichment throughout the rim and flank interval. Note the low-resistivity zone on the deep resistivity (DRES) curves in T-3938 and T-3948 at the base of the apron. Also note the similarities in the FMI facies and gamma-ray logs in T-6337 and the interpreted apron sections in T-5660 and T-5059 from the accretionary sector (Figures 17, 19). For FMI facies definitions, see Figure 10.

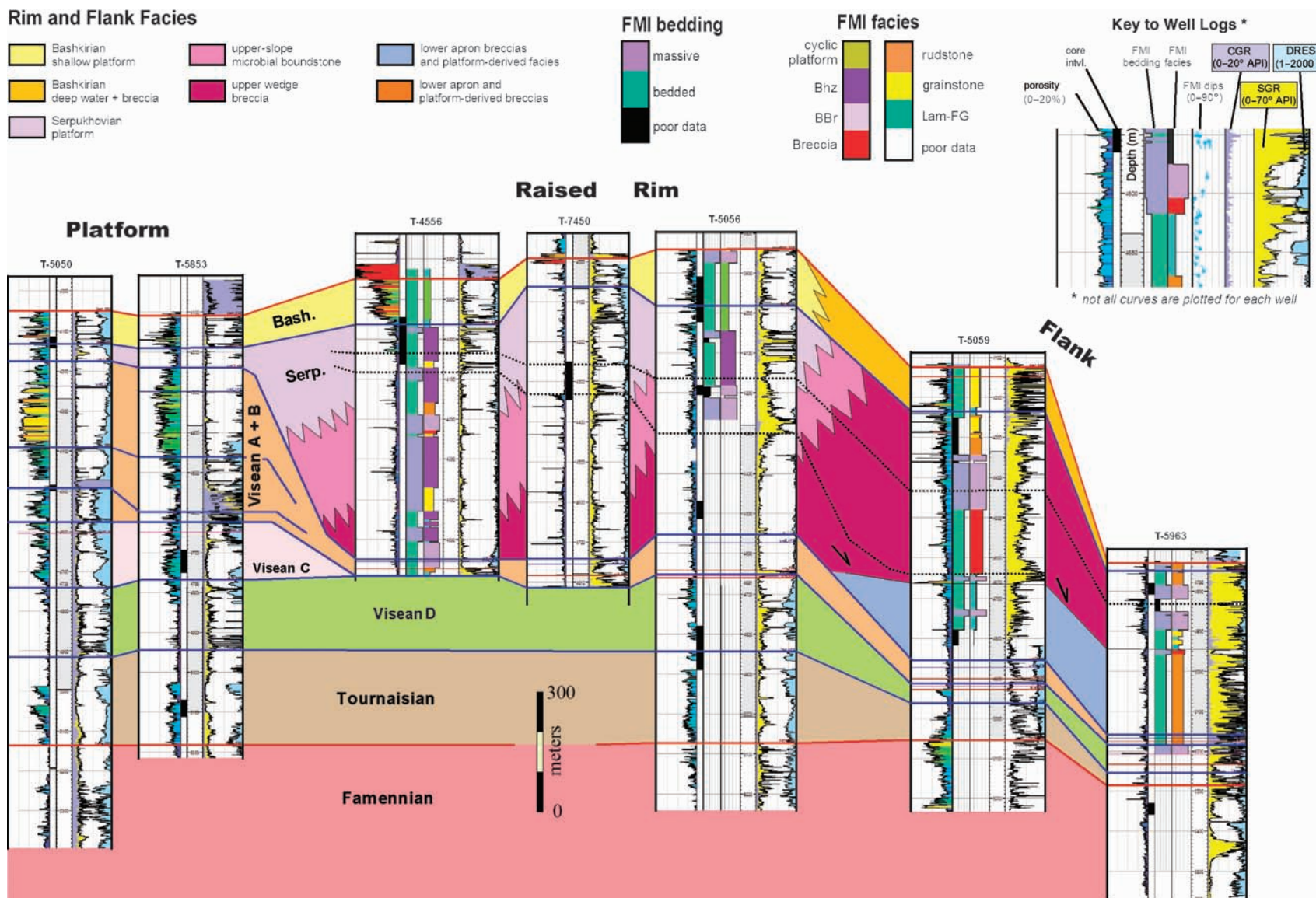


**FIGURE 19.** Stratigraphic and facies relationships in the accretionary rim sector. Wells are shown in order of increasing distance from the platform (see Figure 16 for well locations). Raised rim wells contain Serpukhovian middle-slope breccia and upper-slope boundstone overlain by upper Serpukhovian to Bashkirian outer- and shallow-platform facies. Wells closer to the platform (T-4556 and T-7450) are associated with reduced uranium enrichment, as shown by comparing the spectral gamma ray (SGR) with the computed gamma ray (CGR, calculated with uranium subtracted). Uranium enrichment also tends to be higher in upper wedge boundstone breccia and associated facies in flank wells, above the apron facies interpreted in T-5059 and T-5963. FMI facies and deep-resistivity (DRES) logs are shown for some wells. For FMI facies definitions, see Figure 10.

range (Appendix 2); thus, prebitumen cementation was completed shortly before hydrothermal temperatures were achieved in the reservoir. Equant calcite is a volumetrically important cement in the rim and flank and is referred to as 90° calcite on the basis of the fluid-inclusion data.

### **Fractures and Later Dissolution (Corrosion)**

Larger fractures observed in core can be separated into sets according to their fill phases. Earlier fractures, like early dissolution voids, are extensively filled with prebitumen cement phases. Later fractures contain only bitumen, or equant calcite accompanied by bitumen, and are filled to partly open. Systematic frac-

tures that are mainly open and lack cement are present, representing an even later generation following bitumen deposition, and at least one set of fractures appears to be aligned with the present-day stress regime (D. G. Carpenter, 2005, personal communication). Partly open and open fractures are commonly associated with local solution enlargement along fracture walls, and with bitumen cementation and corrosion in the surrounding rock matrix. Matrix corrosion occurs as microporosity in the micritic components of the rock, for example, skeletal grains and microbial fabrics (Figure 21A). In facies containing micritic matrix, microporosity accompanied by small vugs can sometimes be extensively developed. In addition to

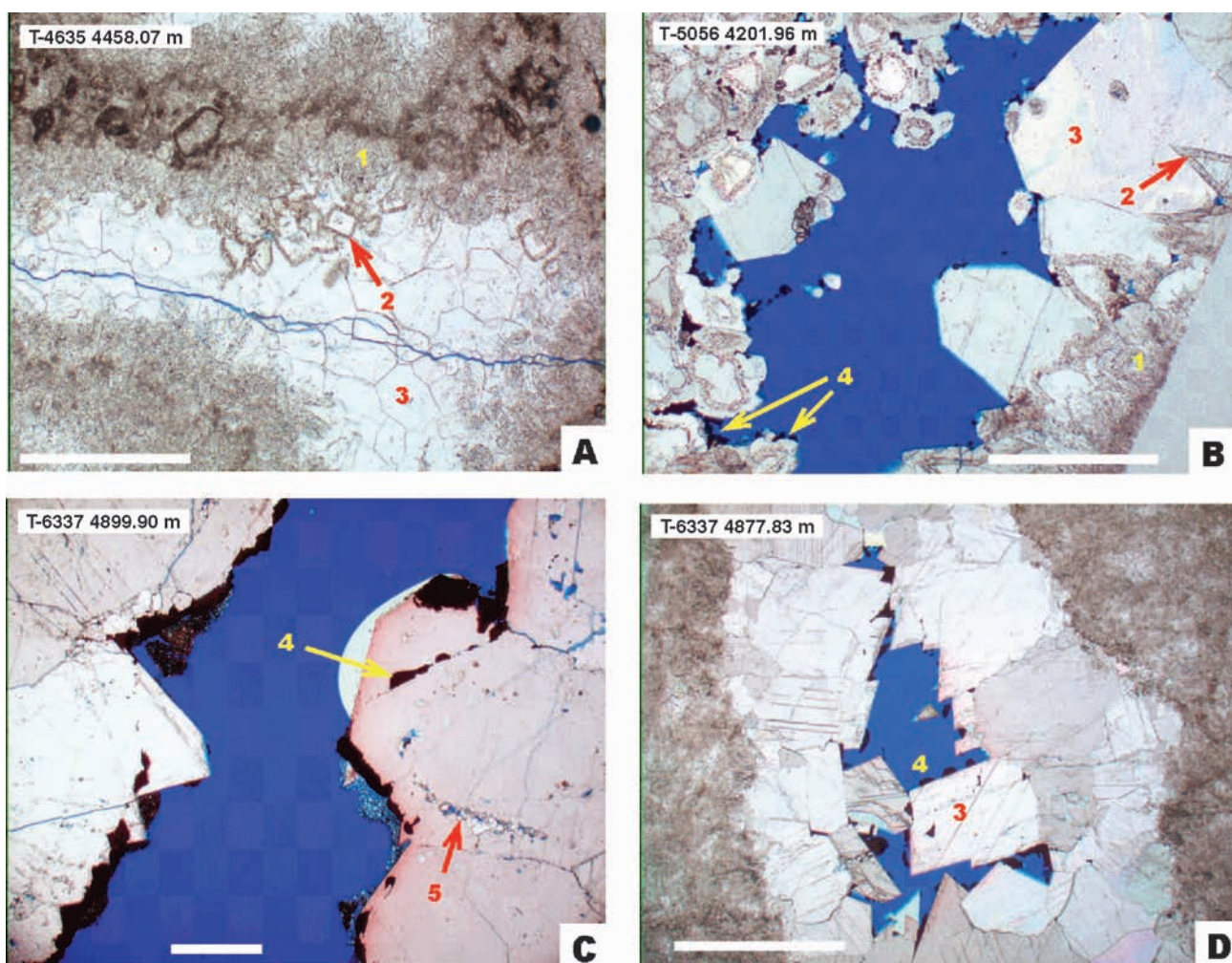


**FIGURE 20.** Earlier stages of diagenesis in the Tengiz rim and flank. Voids are filled by a prebitumen cement sequence (A and B) that includes inclusion-rich, probably marine calcite (1), prismatic to equant zoned calcite and inclusion-rich dolomite (2), and clear blocky equant calcite (3). This sequence is commonly followed by bitumen (4). Prebitumen cements filled much of the primary pore space, as well as porosity created during early diagenetic dissolution and fracturing. Some voids are filled only with equant calcite and bitumen (C and D), indicating a separate, later fracturing and dissolution event. Even later dissolution is suggested by corrosion along crystal growth planes (5) in the equant calcite. Fluid-inclusion homogenization temperatures of 80–95°C for the equant calcite indicate the existence of prehydrothermal conditions in the reservoir prior to bitumen formation. Scale bars = 1 mm.

matrix corrosion adjacent to solution-enlarged fractures, bitumen and corrosion are noted between cements and walls of partly filled fractures. Bitumen and corrosion are also sometimes observed within inclusion-rich prebitumen cements or along cleavage and growth planes of individual cement crystals.

Bitumen and matrix corrosion are both observed to decrease away from vugs and enlarged fractures, suggesting that bitumen, corrosion, and large-scale dissolution may be genetically linked. Petrographic observations indicate that significant corrosion and solution enlargement postdates the early cement sequence. A key question is whether most of this occurred before, during, or after bitumen formation or a combination of the three. Examples where bitumen-associated

microporosity and bitumen-free microporosity occur in the same thin section are common (Figure 21B), and in some cases, dissolution is observed that appears to post-date bitumen formation (Figure 21C). This suggests that some matrix corrosion probably accompanied bitumen emplacement, and that some dissolution may also have occurred later along the same pathways. However, many other instances indicate mainly passive fill of open void space by bitumen, accompanied by only minor micrite corrosion.

Other postbitumen diagenesis includes fractures, noncarbonate cement such as fluorite and quartz (based on fluid-inclusion temperatures; see Appendix 2), and possibly some calcite spar (Figure 21D). The existence of syn- and postbitumen cementation and dissolution

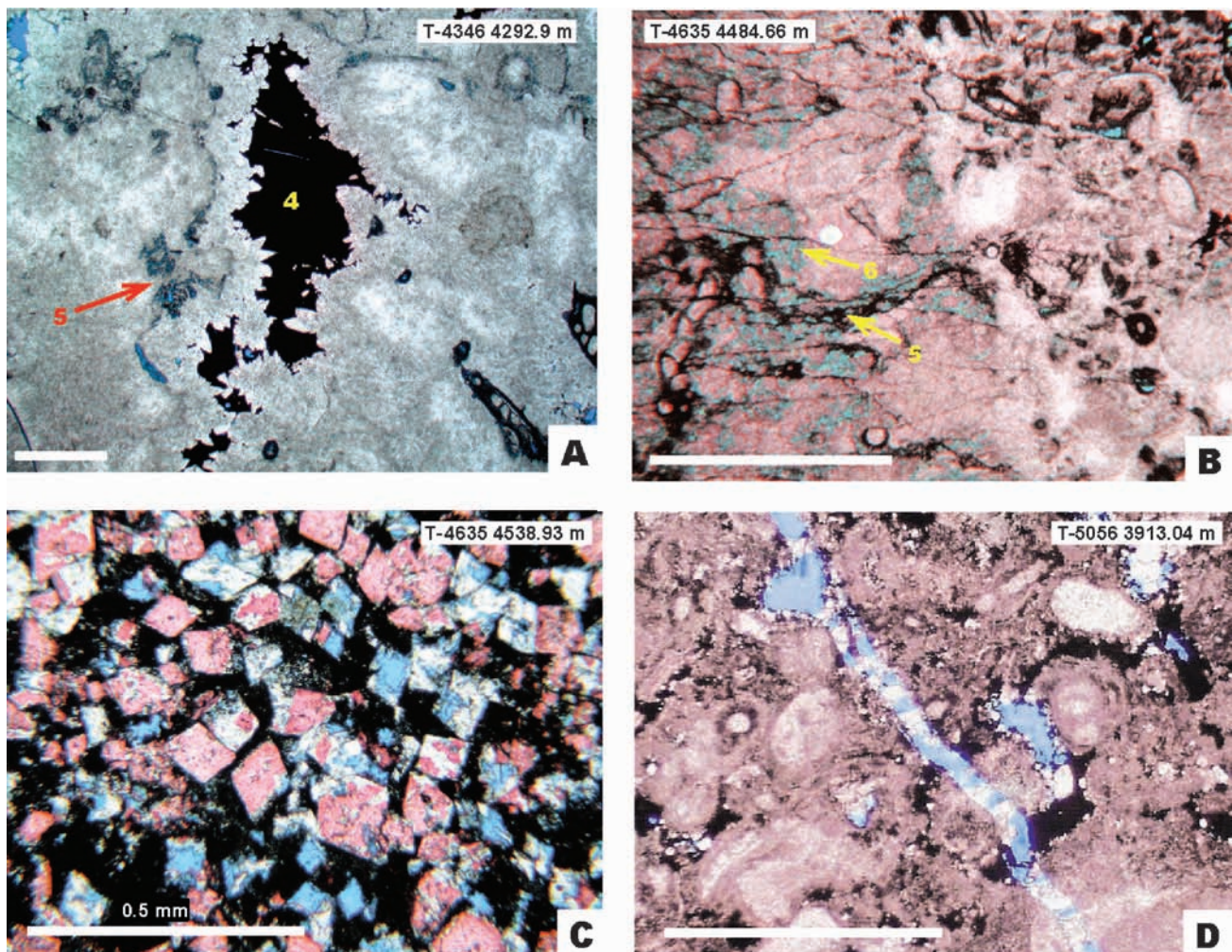


**FIGURE 21.** Bitumen-related and postbitumen diagenesis in the Tengiz rim and flank. Bitumen is dominant in some voids and fractures (A, 4) and is commonly associated with corrosion of microbial fabrics (A, 5). Some micrite corrosion appears to be free of bitumen (B, 6) and possibly postdates bitumen formation. Postbitumen diagenesis also includes dissolution (selective dissolution of dolomite rhombs in a partial dedolomite, C) and late fracturing (D). The example in (D) also shows postbitumen calcite cement. A key question in the Tengiz rim and flank is how much postbitumen dissolution and fracturing contributes to present-day reservoir quality and distribution. Scale bars = 1 mm, except where indicated.

implies that an active hydrothermal system was probably a factor in the development of the rim and flank reservoir. Two scenarios are proposed: hydrothermal fluid mixing and geothermal convection. Mechanisms for hydrothermal mixing includes fluids with different  $H_2S$  concentrations or thermochemical sulfate reduction (TSR) reactions between hydrocarbons and sulfate minerals. These possibilities are suggested by:

- 1) the elevated  $H_2S$  content (13%) of hydrocarbons in the reservoir
- 2) the presence of known TSR byproducts in the reservoir
- 3) the thermal regime, estimated from fluid-inclusion studies, under which these products were precipitated
- 4) the presence near or within the reservoir of geological conditions and ingredients favorable for TSR reactions.

Geothermal convection is supported by two-dimensional numerical flow models of Tengiz using temperatures derived from basin modeling, known thermal rock and fluid properties, and a simplified layering scheme based on bulk reservoir permeabilities. It is also possible that both convective and  $H_2S$ -related processes contributed to rim diagenesis and reservoir quality at different times or at the same time.

### ***Hydrothermal Fluid Mixing and $H_2S$ -related Diagenesis***

According to basin models, the Tengiz reservoir attained hydrothermal temperatures during the early stages of post-Triassic rapid subsidence (Figure 22). During and after this time, basin-generated hydrothermal fluids may have periodically charged the reservoir, mixing with formation fluids. Thin sections and quantitative x-ray diffraction data from core plugs reveal the presence of anhydrite, dolomite, chalcedony, quartz, barite, fluorite, fluorapatite, and pyrite as potential hydrothermal species in the rim and flank. Most of these minerals exist in quantities less than 4% by weight. Species that may have a hydrothermal origin and have been measured as much as 50% and higher by weight in individual samples include fluorapatite, anhydrite, and dolomite (anhydrite and dolomite may also have other origins). Chalcedony and quartz are also locally abundant. Homogenization temperatures of 110–125°C have been obtained from examples of quartz and fluorite (Appendix 2).

Significant calcium carbonate dissolution can occur in reservoirs where fluids with different  $H_2S$

saturations are mixed (Hill, 1995), or when  $H_2S$  and  $CO_2$  generated by TSR mix with oxygenated formation water in a carbonate reservoir (for example, see Hill, 1990). In the absence of oxygenated formation waters, the amount of carbonate dissolution that occurs in the presence of  $H_2S$  and  $CO_2$  is controlled by pH of the formation waters and the presence of iron oxides or aqueous sulfides (Stoessel, 1992). Carbonate dissolution commonly occurs because of carbonic and/or sulfuric acid generated during these reactions (Hill, 1987; Machel, 1987, 1989). Once  $H_2S$  saturation became established in the reservoir, either by migration of  $H_2S$  and  $CO_2$  gases or after migration of hydrocarbons, additional dissolution may have occurred as a result of periodic mixing with external hydrothermal fluids during even later burial.

The high burial temperatures, elevated  $H_2S$  levels, and the presence of bitumen, dedolomite, and anhydrite suggest the possible involvement of TSR in diagenesis of the rim reservoir. In the Tengiz region, potential reactants include hydrocarbons generated from Carboniferous to Permian subsalt source rocks adjacent to the buildups (Lisovsky et al., 1992) and an anhydrite layer at the base of the thick Permian halite formation that encases the buildups. Figure 23 shows two possible regions where reactions might have occurred:

- 1) basinal areas between platforms where hydrocarbons were being generated; in this scenario, carbonate dissolution occurred after migration of  $H_2S$  and  $CO_2$  from reaction sites into the reservoir
- 2) in the reservoir itself, with carbonate dissolution resulting from reactions that occurred when liquid hydrocarbons entered the reservoir

The latter mechanism is possible because the absence of Moscovian–Artinskian volcanics on the upper slope of the Tengiz flank places the anhydrite layer in direct contact with the reservoir. It has the advantage of also accounting for, as a common by-product of TSR, at least some of the ubiquitous bitumen in the rim and flank. Reservoir temperatures of 80–95°C achieved prior to bitumen emplacement (based on prebitumen equant calcite) indicate that bitumen formation probably occurred as the reservoir entered the hydrothermal regime.

Carbonate reservoirs exposed to TSR commonly contain anhydrite, dedolomite, sulfide minerals, elemental sulfur, and uranium and iron enrichment (Hill, 1990, 1995). In particular, anhydrite and dedolomite of apparent nonevaporative or nonsubaerial origin are commonly observed in cores and thin sections

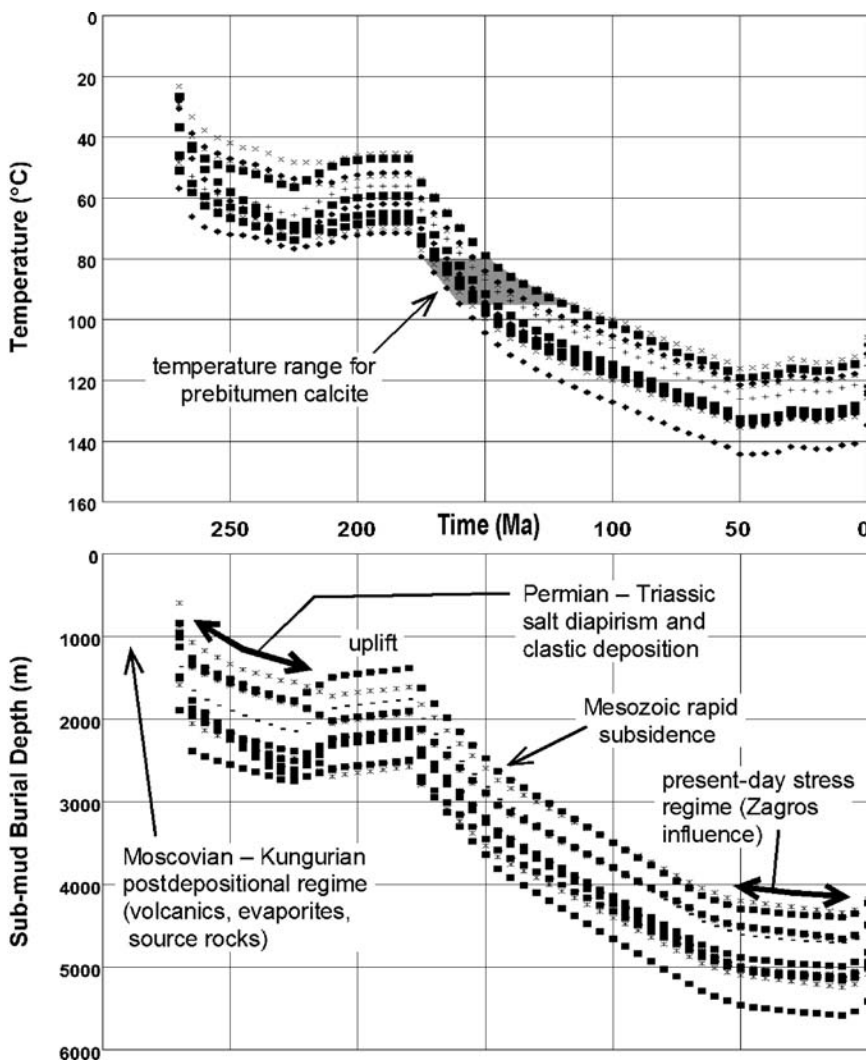


**FIGURE 22.** Temperature and burial-history plots for the Tengiz rim and flank reservoir from basin modeling. The vertical depth range indicates the suite of samples from different parts of the reservoir interval used in fluid-inclusion analyses (Appendix 2). Bitumen formation in the reservoir began, probably under hydrothermal conditions, after cementation by equant calcite (top) during Mesozoic subsidence. Potential times of burial fracture generation include stresses generated during salt diapirism, uplift (approximately 220–175 Ma), rapid Mesozoic subsidence, and the present-day stress regime (bottom).

from the Tengiz rim, and GR logs from rim and flank penetrations typically show uranium enrichment (see Figures 18, 19). The presence of dedolomite suggests the involvement of fluids with excess  $\text{Ca}^{2+}$ , possibly from TSR-related anhydrite dissolution.

### Geothermal Convection

Groundwater circulation can be important in the diagenetic history of carbonate reservoirs, particularly for isolated platforms (Jones et al., 2004). Platform margins are favorable sites for convective circulation during burial, as well as during deposition. Depositional or early postdepositional convective processes were previously briefly cited with respect to early dissolution at the Tengiz margin. Geothermal convection can occur during burial under certain conditions (Machel and Anderson, 1989; Morrow, 1998; Wendte et al., 1998; Heydari, 2000). Two-dimensional numerical fluid-flow simulations indicate that large-scale geothermal convection is feasible in the Tengiz

rim and flank (G. D. Jones and Y. Xiao, 2005, personal communication), mostly because of the high vertical permeability possible in fractured reservoirs and because of a relatively large center-to-edge temperature gradient in the buildup caused by the thick, conductive envelope of halite around the exterior.

Once convection cells are established in a closed system, areas of net dissolution and net cementation can occur while maintaining average saturation equilibrium in the cell with respect to the reservoir. Because of the inverse relationship at constant pH and  $p\text{CO}_2$  between calcium carbonate solubility and temperature, dissolution occurs where saturated or nearly saturated fluids are cooling (rising cell limbs), and cementation occurs where such fluids are warming (descending limbs). However, this process results in mass transfer of carbonate from one area to another, and closed-system cells may, over time, be forced to readjust in shape or shut down in response to changing permeability patterns.

Numerical models further indicate that convection cells, if they remain active long enough, can transfer sufficient calcium carbonate to significantly affect porosity in the reservoir (G. D. Jones, 2005, personal communication). Several factors may have facilitated long-term active convection in the rim and flank of Tengiz. The absence of Moscovian to Artinskian sediments on the upper slope of Tengiz (Figure 23) may have allowed continuous seawater exchange for rim and flank convection throughout an extended period following deposition. Second, Tengiz appears to have

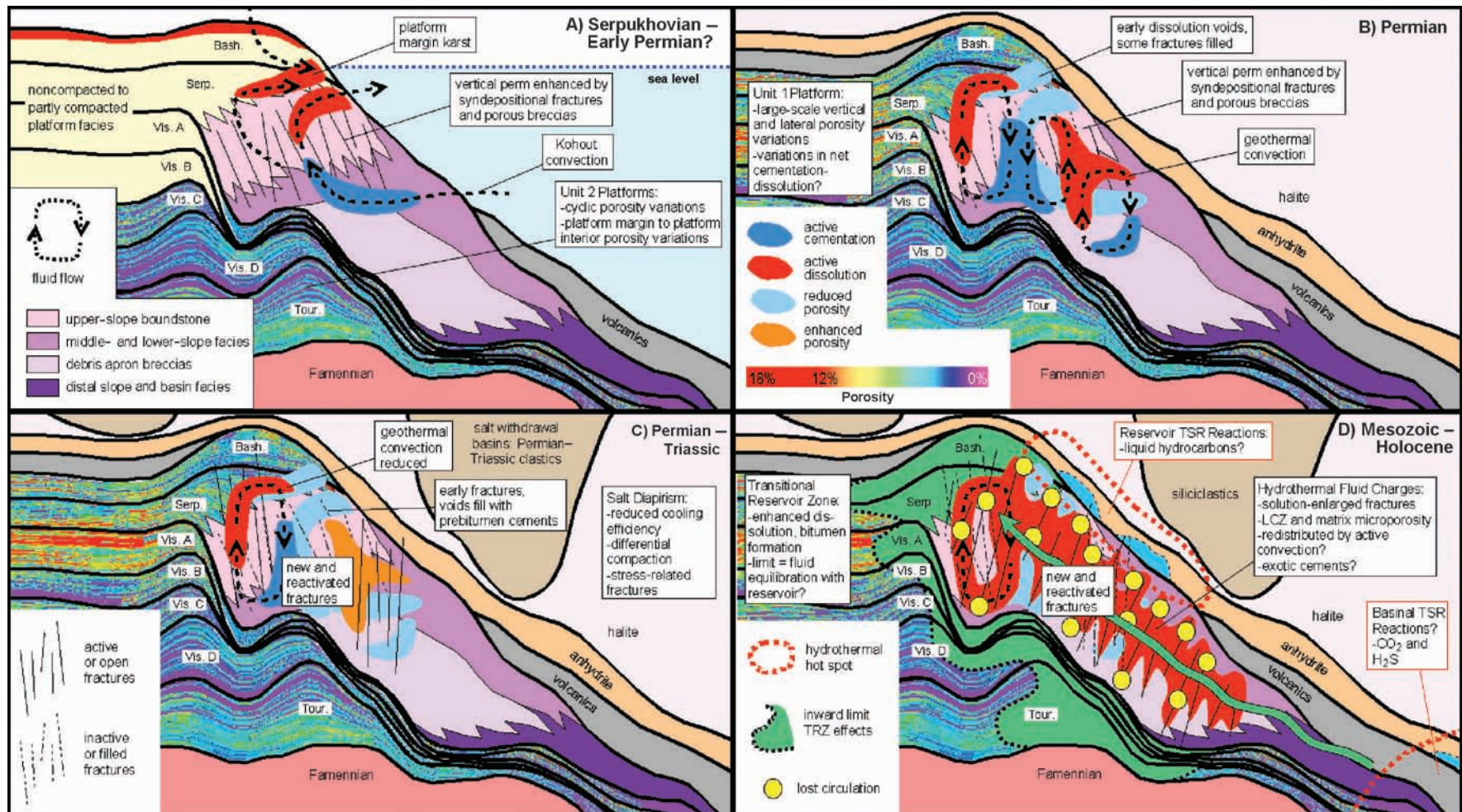


**FIGURE 23.** Evolution of the Tengiz rim and flank high-permeability reservoir, based on data and analyses contained in the text. Prior to burial (A), the reservoir consisted of fractures and large vugs caused by syndepositional instability and platform margin karsts. Initial large-scale dissolution and cementation patterns may have been controlled by Kohout convection and by meteoric and mixing processes. During early burial (B), they may have been controlled by geothermal convection, promoted by still-open fractures and by deposition of thermally conductive halite. Conductivity loss and differential compaction caused by salt diapirism may have reduced or eliminated geothermal convection (C), although compactional stresses may have rejuvenated the fracture system. Prebitumen cements may have significantly reduced nonmatrix porosity and permeability by the end of this stage. New tectonic stresses again reactivated the fracture system, possibly facilitating movement and distribution of hydrothermal fluids in the reservoir (D). Diagenesis related to thermochemical sulfate reduction (TSR) is believed mainly responsible for solution enlargement of open fractures and lost circulation zones (LCZ), either from migration of CO<sub>2</sub> and H<sub>2</sub>S gas, or as a direct result of the liquid hydrocarbon charge. These fluid charges may also be responsible for enhanced dissolution in adjacent platform facies, forming the transitional reservoir zone (TRZ). Note that overall fracture density, but not necessarily openness, increased in reservoir over time.

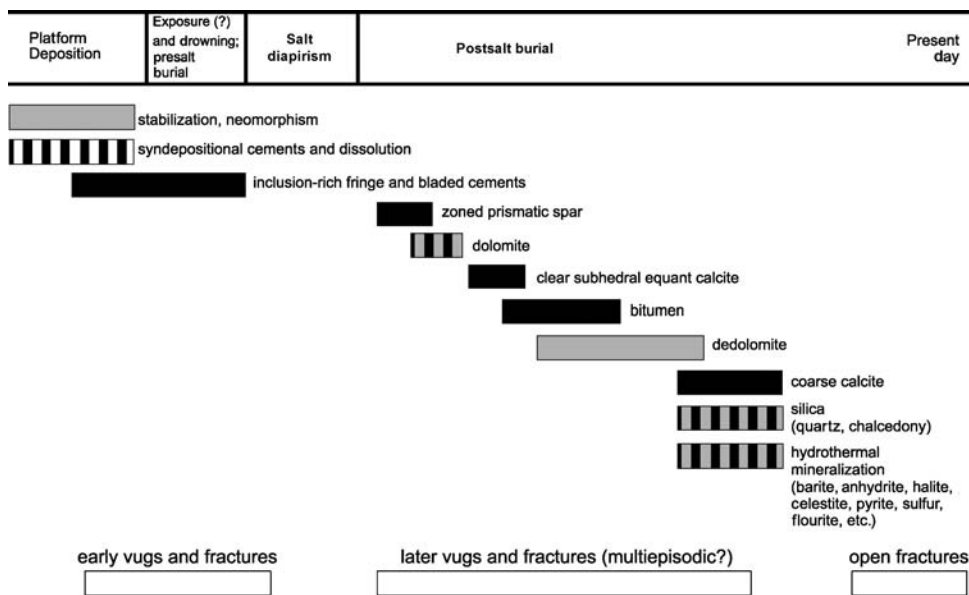


**FIGURE 24.** Tengiz rim and flank paragenesis. Cementation events are indicated in black, dissolution events are indicated in white, and events that involve mainly replacement or recrystallization are shown in gray. Approximate absolute timing has been established for zoned prismatic spar, dolomite cement, and subhedral equant calcite ( $150 \pm 25$  Ma; see Figure 22) from fluid-inclusion results. Based on petrographic relationships, these cements were emplaced just prior to bitumen deposition (see Figure 20) and the time when hydrothermal temperatures were attained in the reservoir. All other diagenetic products are shown in relative order only, as part of either the prebitumen or postbitumen sequences. Other phases might be constrained by processes related to burial history, which has an implied time scale (see Figures 22, 23).

had a complex fracture history (Figure 24). Multiple fracture events and/or repeated reactivation of previous fractures in the rim and flank may have maintained or increased vertical permeability over time, allowing geothermal convection to remain active during burial.

## RESERVOIR QUALITY AND DISTRIBUTION

The distribution of reservoir rock types in carbonate reservoirs is a product of interactions between depositional facies and diagenetic processes. Reservoir quality should tend to average out somewhat when comparing deeper well penetrations or wells from the same environment in the field because these wells encounter a wider range of stratigraphic ages, facies, and potential diagenetic themes in the Tengiz spectrum. Reservoir quality at Tengiz has so far shown a stronger relationship to specific well locations than to facies or stratigraphy. A partial explanation for these geography-based reservoir-quality variations lies in understanding the relative contributions of dissolution, cementation, and fracturing to matrix and nonmatrix porosity in the outer platform, rim, and flank. Because of the significant contribution of nonmatrix

porosity (fractures, large vugs, and lost circulation zones) in some facies, the rim and flank are considered a dual-porosity reservoir. Different reservoir facies in the rim and flank can be recognized based on both matrix and nonmatrix pore types.

### Matrix Reservoir Types

Air permeability data combined with thin sections from core plugs were used to guide the recognition of matrix reservoir rock types in the Tengiz rim and flank. This data, while not quantitatively accurate for characterization at reservoir conditions, nevertheless represent a relatively consistent laboratory test that is useful for distinguishing reservoir rock types based solely on rock properties. The classification scheme used for analysis of Tengiz plugs was modified from that of Lucia (1999) and recognizes five matrix pore-type classes (interparticle porosity, microporosity, touching vugs, separate vugs, and fractures) based on independent permeability behavior as a function of porosity. Applied to Tengiz, these data permit the distinction of three main reservoirs based on matrix properties:

1) The rim and flank reservoir (Figure 25) encompasses upper-, middle-, and lower-slope facies containing mainly microbial boundstone or breccia (but also including some interbedded platform-derived facies).

- 2) The transitional reservoir zone (Figure 26) consists of shallow-platform or outer-platform facies with significant bitumen cement and matrix dissolution. This term is used instead of outer platform because the reservoir type is not restricted to that facies. It should not be confused with the term "transition zone," commonly used to describe certain conditions in hydrocarbon columns.
- 3) The central platform reservoir includes the central regions of the Tengiz platform that are

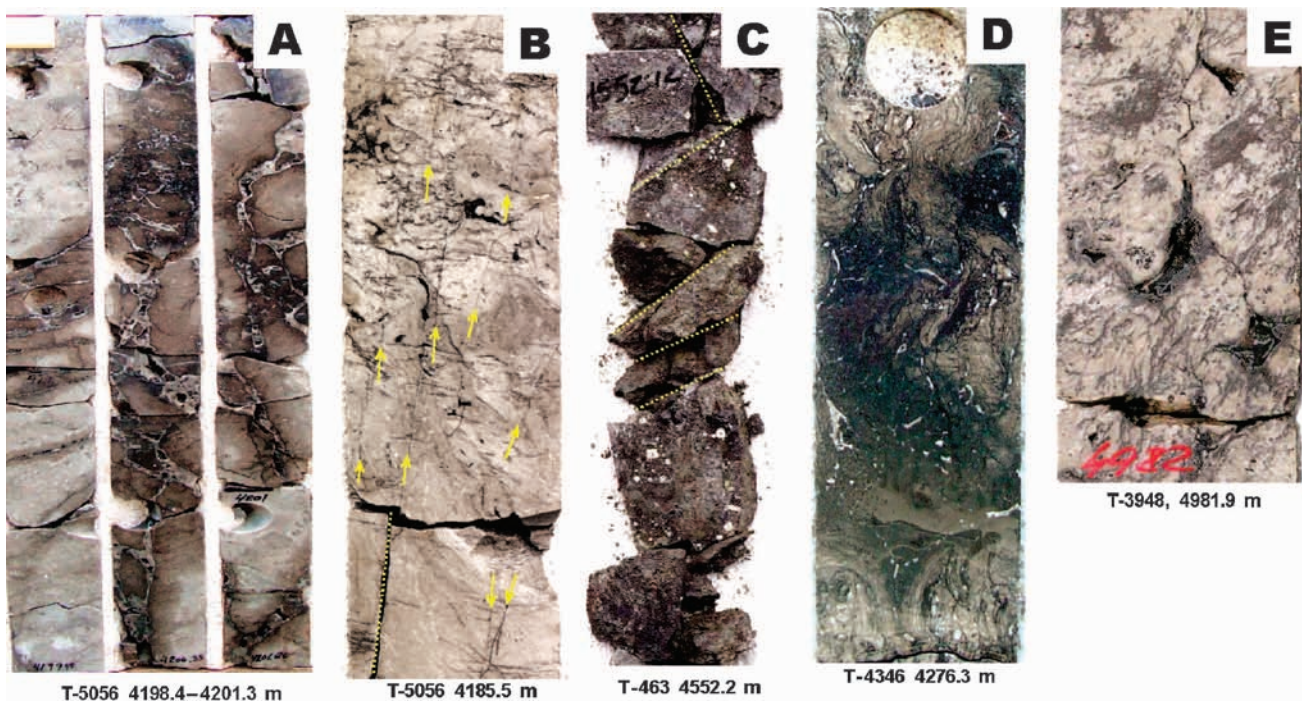


**FIGURE 25.** General characteristics of the rim and flank reservoir. (A) Local solution enlargement of a partly cemented fracture-breccia in microbial boundstone. Dissolution is found along the fracture walls and between cement crystals. Bitumen-filled microporosity (darker color) extends a few centimeters from the fractures, but matrix porosity is otherwise low. A lost circulation zone is associated with this feature. (B) Microbial boundstone with low matrix porosity and systematic bitumen-filled hairline fractures. (C) Probable fractured zone in skeletal-lithoclast rudstone with extensive matrix corrosion, resulting in core rubble. The dark color is caused by pervasive bitumen cementation. (D) Microbial boundstone (clast in breccia) with bitumen and microporosity developed along microbial filaments. (E) Microbial boundstone (clast in breccia) with vugs formed by localized solution enlargement between microbial masses.

relatively unaffected by bitumen plugging and associated effects (see Kenter et al., 2006).

It can be demonstrated that much of the Viséan A, Serpukhovian, and Bashkirian platform reservoir is in pressure communication with the rim and flank. As shown in Figure 23, the transitional reservoir zone refers to parts of the outer regions of these platforms that may have been altered by the incursion of various diagenetic fluids active in the rim. For example, the extent of this region may represent the equilibration limit of corrosive hydrothermal fluids that charged the reservoir or the innermost edges of active convection cells. The greatest distinction in matrix properties is between the transitional reservoir zone, affected by bitumen plugging and matrix dissolution, and the central platform reservoir (Figure 27). Because similar depositional facies are present in both the outer and central regions for shallow-platform cycles, bitumen and dissolution are mostly responsible for the observed differences. In some cycles, early porosity and permeability in the transitional reservoir zone may have been adversely affected by the presence

of deeper, outer-platform facies or by the presence of microbial or marine cements (for example, see Figure 6). Figure 27 shows a more subtle contrast between the transitional reservoir zone and the rim and flank reservoir. Because bitumen and dissolution affected both of these reservoirs, the difference is more likely caused by the grainy nature of transitional reservoir zone facies, which probably had higher matrix porosity prior to bitumen and dissolution, in contrast with rim and flank facies that are dominated by early-cemented microbial boundstone and boundstone breccia.

### *Transitional Reservoir Zone*

The porosity range for the transitional reservoir zone determined from plug data is intermediate between the central platform range and that of the rim and flank reservoirs (Figure 27A). The data also show a large amount of permeability scatter around the central platform trend (Figure 27B). The transitional reservoir zone matrix is characterized by larger pore sizes because of solution enlargement of early interparticle and moldic porosity and because smaller



**FIGURE 26.** Characteristics of the transitional reservoir zone, which affects the outer regions of the Visean A, Serpukhovian, and Bashkirian platforms. Facies include skeletal packstone-rudstone with brachiopods and large crinoids (D, F, J, and K), sponge or coral boundstone (E and H), and occasional high-energy ooid grainstone (G). These examples have in common dissolution enlargement and bitumen cementation in the matrix. Dissolution enhancement includes matrix vugs (D, arrows) and enlarged fractures or stylolites (D, J, and K). Bitumen (darker colors in core examples) is somewhat fabric selective in (E–H). The example in (F), interpreted as a karst feature, shows differences in relative bitumen abundance relative to the fracture and to the clasts in the cavity. In thin section, bitumen is commonly associated with minor corrosion (cement corrosion in B and C, arrows). Bitumen and solution enlargement have offsetting effects on porosity and permeability, as shown in (A), in which both bitumen-cemented pores (arrows) and solution-enlarged pores are visible.

pores tend to be bitumen filled (Figure 26A, B). Larger pores exhibit only partial fills or incomplete linings. The reduced porosity range in the transitional reservoir zone, thus, appears to be caused by bitumen cementation of smaller pores, whereas the permeability scatter appears to be caused by a combination of bitumen plugging and solution enhancement that resulted in a fundamental change in matrix pore size, shape, and connectivity. For the same porosity value or porosity range, the transitional reservoir zone has slightly better average matrix permeability compared to the central platform reservoir. Thus, whereas bitumen plugging appears to have reduced the porosity range in the transitional reservoir zone, an expected reduction in permeability over that range has been offset by dissolution.

Because significant matrix porosity likely remained in the transitional reservoir zone after depositional and early diagenetic processes, cyclic controls on platform porosity probably influenced patterns of later dissolution and cementation. The net effect of porosity changes caused by bitumen plugging and matrix dissolution overprinted across facies results in a noticeable change in the expression of cyclicity

on porosity logs. In particular, dissolution somewhat disguises the loss of porosity observed at sequence boundaries in the central platform (Kenter et al., 2006) and adds high-frequency vertical porosity variations in the cycles. Log character thus provides a means of constraining the width of the transitional reservoir zone along the outer edge of the platform. Based on current well and core control, the width appears to vary vertically and may range from less than 500 m (1640 ft) to more than 2 km (1.2 mi).

### Rim and Flank Reservoir

The data from the rim and flank reservoir in Figure 27 indicate a further reduction in matrix porosity range but permeability scatter similar to the transitional reservoir zone. Although it was originally anticipated that matrix reservoir quality might depend on the amount of grainy matrix in different facies, comparisons of matrix-rich breccias, more tightly packed breccias containing little or no matrix, and in-situ microbial boundstones do not reveal greatly different porosity ranges (Figure 28). It is also surprising, given that matrix dissolution features are less

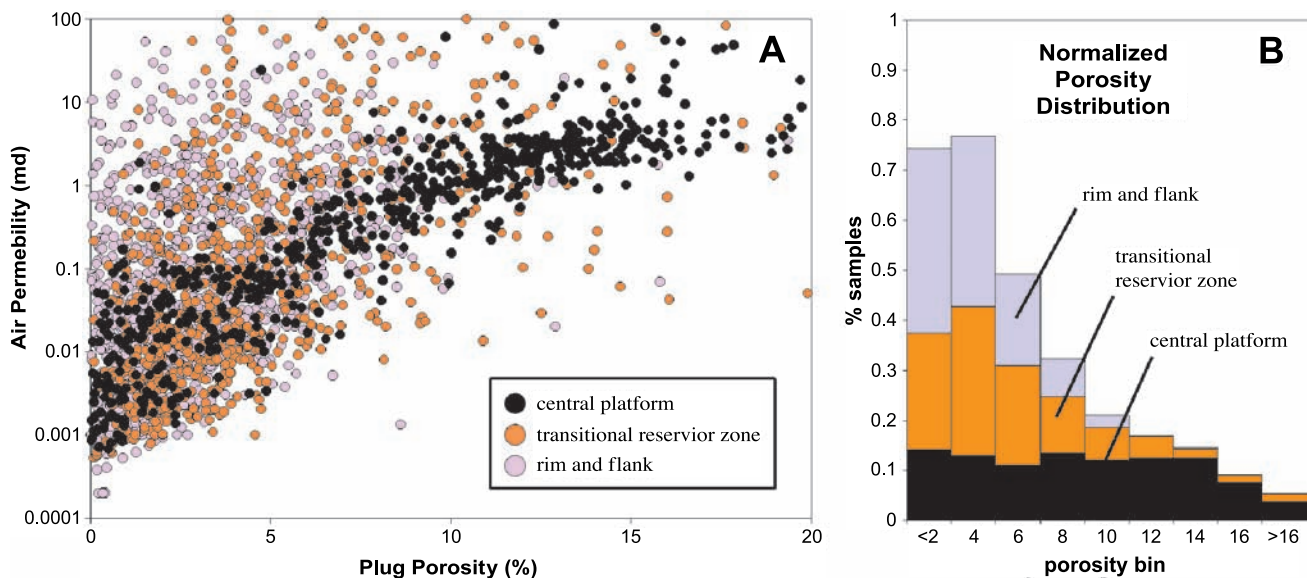


**FIGURE 27.** Plug porosity and permeability data comparing the matrix reservoir from the central platform, transitional reservoir zone (TRZ), and rim and flank areas. The central platform trend includes almost 5000 plugs (only a partial set is plotted) and demonstrates a single trend despite a variety of facies, textures, and reservoir rock types represented. The rest of the data consists of approximately 1700 plugs from the rim and flank and 700 from Bashkirian and Serpukhovian outer-platform facies representing the TRZ. Increased permeability scatter and reduced porosity ranges characterize both the TRZ and the rim and flank trends compared to the central platform (A). In the TRZ, reduced porosity is caused mainly by bitumen, whereas the permeability scatter is caused by a change in pore connectivity from the combination of bitumen plugging and solution enlargement. In the rim and flank, the porosity range is reduced further (B), because of the presence of tightly cemented microbial boundstone facies. The permeability scatter is partly a function of solution-enlarged pores, but also because of the increased importance of vuggy-moldic pore types and microfracture porosity.

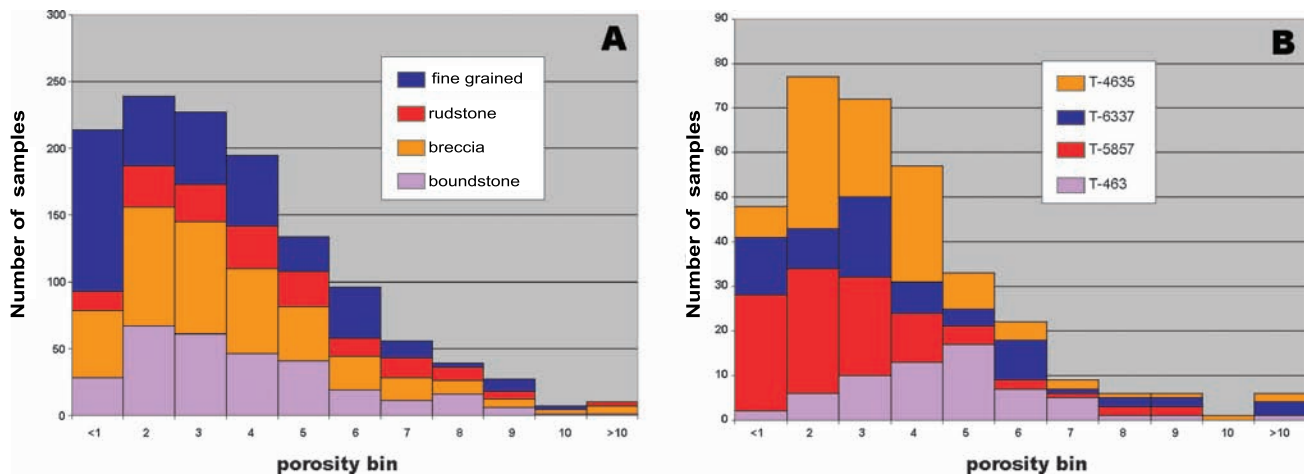


**FIGURE 28.** Histograms from plug data comparing matrix porosity ranges in the rim and flank by facies (A) and by well (B). Boundstones and breccias have similar distributions, rudstones have slightly better porosity (based on higher frequency in the 3–5% bins), whereas fine-grained platform-derived facies have a lower porosity range. Overall, however, porosity variability between facies is instead weak compared to the variations by well, suggesting a strong diagenetic overprint.

abundant overall and appear to be more poorly connected, that rim and flank matrix permeability is comparable to that of the transitional reservoir zone. This may be partly an artifact of the increased abundance of small fractures, producing a greater amount of plug damage. However, dissolution is observed along some small fractures in plugs, so whereas the number of plugs with high permeability may be inflated, the range is probably real. It should also be remembered that these are comparative statistical relationships that only apply where matrix porosity exists and cannot be extrapolated to generalizations about the overall distribution of porosity.

Porosity in upper- and middle-slope microbial boundstones and breccias was substantially reduced by sediment fill and prebitumen cementation of early pore types. These include fenestrae, microbial growth and framework cavities, and other primary voids, as well as early fractures and dissolution voids. In middle- to lower-slope and apron facies, it was expected that the presence of skeletal rudstones or floatbreccias with grainy matrix might improve reservoir quality in some areas because of possible preservation of primary porosity, compared to areas containing tightly packed breccias or breccias with finer grained or micritic matrix. However, like the upper slope, matrix reservoir quality in most middle- to lower-slope facies is affected by bitumen, corrosion, and prebitumen cement, in particular syntaxial calcite (of probable early to moderate burial origin) and clear equant calcite (including 90° calcite of burial origin). Early marine cements prevalent in the

upper-slope facies are less noticeable. Burial cementation and dissolution processes may be part of the reason why there is no good evidence that breccias, in general, have better reservoir quality compared to other facies, or that better reservoir quality is associated with a particular type of breccia.

#### *Matrix and Nonmatrix Reservoir Distribution*

Nonmatrix features consisting of fractures, large vugs, and lost circulation zones are an important component of the rim and flank reservoirs. These elements are absent or greatly reduced by comparison in the central platform area. The distribution of these features and their relationships to matrix properties are the basis of rim and flank reservoir characterization. As described previously, open fractures, vugs, and lost circulation zones appear to be linked to areas of bitumen cementation and solution enlargement (see Figure 25). Whereas bitumen is associated with dissolution along fractures and in the surrounding matrix, it is also responsible for plugging up some fractures and vugs. Furthermore, bitumen and dissolution affect matrix reservoir quality to varying degrees in fractured intervals, and matrix dissolution and bitumen can sometimes be more extensively developed in areas of lower fracture density. Understanding these variations in spatial and genetic relationships is a key to improved reservoir-quality prediction.

Bitumen-associated matrix dissolution includes microporosity, micrite corrosion, vugs, and enlarged primary voids. In detrital middle- to lower-slope and

apron breccias, residual matrix porosity controlled by primary texture and prebitumen cementation appears to have regulated the extent to which matrix corrosion is developed locally. Incompletely cemented grainy facies lend themselves to more extensive corrosion, and small-scale variations in these parameters sometimes result in apparent bedding or facies control, obscuring a relationship to larger scale fracture density. In upper-slope boundstones and breccias, microporosity occurs mainly in primary microbial fabrics and entrained micritic skeletal grains. Because little or no matrix is present in these rocks, a general relationship to open and partly open fractures is more clearly evident. The amount of matrix corrosion and dissolution that develops depends on the type of boundstone (which, in turn, determines the density of entrained grains and microbial fabrics) and on the amount of prebitumen cement (commonly abundant because of high volumes of marine cement). Whereas this combination can produce a complex-looking distribution of corrosion and bitumen relative to primary textures in boundstones and breccias, a clear spatial connection exists between the matrix and nonmatrix components of bitumen and associated dissolution, and variations in matrix components are determined more by prebitumen cementation patterns than by fracture density or facies.

### ***Early Karst Features***

Early karst features are commonly cited as important influences on porosity and permeability distribution in carbonate reservoirs. The overall effect may be positive or negative (Esteban and Wilson, 1993; Wagner et al., 1995). Early karst features can vary considerably in spatial distribution and relationship to stratigraphy (for example, Choquette and James, 1987; Lucia, 1995; Mylroie and Carew, 1995), although for isolated platforms, dissolution is commonly concentrated near the platform margin (for example, Cander, 1995; Tinker et al., 1995). Early karsts may also influence later diagenesis, serving as targets for selective re-excavation or forming significant impediments to later fluid flow (Ford, 1995). Large-scale features interpreted as early karst are present at Tengiz; however, observed relationships between these features, the distribution of later diagenetic features (bitumen cement and corrosion), and overall porosity and permeability suggest that early karsts are largely incidental to reservoir quality.

Potential early karst features include local subaerial exposure effects associated with sequence boundaries, brecciated intervals, and large, sediment-filled

cavities (Figure 29). Almost all of these features are completely filled with sediment and, to a lesser extent, cement. Later bitumen and corrosive diagenesis are present in these intervals and, in some cases, are even concentrated within or around the karst or dissolution features (Figure 29A). However, when compared to randomly selected cored intervals or to cored intervals of equal thickness where similar features are absent, the intervals containing the karst features tend to have, on average, diminished amounts of bitumen and dissolution, and average reservoir quality in these zones does not appear to be consistently better or worse than elsewhere.

### ***Lost Circulation Zones***

Lost circulation during drilling in the rim and flank can be shown to occur in association with increased open-fracture density or with solution enlargement of fractures in instances where FMI control, or in some cases, core control, exists. Recent drilling without catastrophic losses and with more complete core recoveries in intervals dominated by vuggy porosity further suggests that perhaps the distribution of fractures or solution-enlarged fractures are the most significant controls on lost circulation in general. Because solution-enlarged fractures are commonly associated with areas of dissolution, corrosion, and bitumen, an important question is whether fracture distribution was the primary control on where solution enlargement and lost circulation occurred, or whether the distribution of corrosion and dissolution, constrained by other factors, determined where fracture enlargement and lost circulation occurred. Ultimately, the distribution of lost circulation zones in the rim and flank may indicate specific pathways through the reservoir taken by corrosive fluids or map out areas of elevated fracture density.

As previously outlined, different fracture sets in the Tengiz rim and flank can be distinguished by orientation relative to core, by types of fill, and by the amount of dissolution. Possible origins are varied, including syndepositional instability, burial stresses created by differential compaction of the rim and platform areas (and, to a lesser extent, the rim and flank areas), differential stresses resulting from overburden loading during salt diapirism, and stresses associated with various tectonic events affecting the Precaspian Basin (D. G. Carpenter, 2005, personal communication). Fracture density controlled by the mechanical properties of different facies is one possible influence on the current distribution of lost circulation zones. Both core and FMI data show that microbial

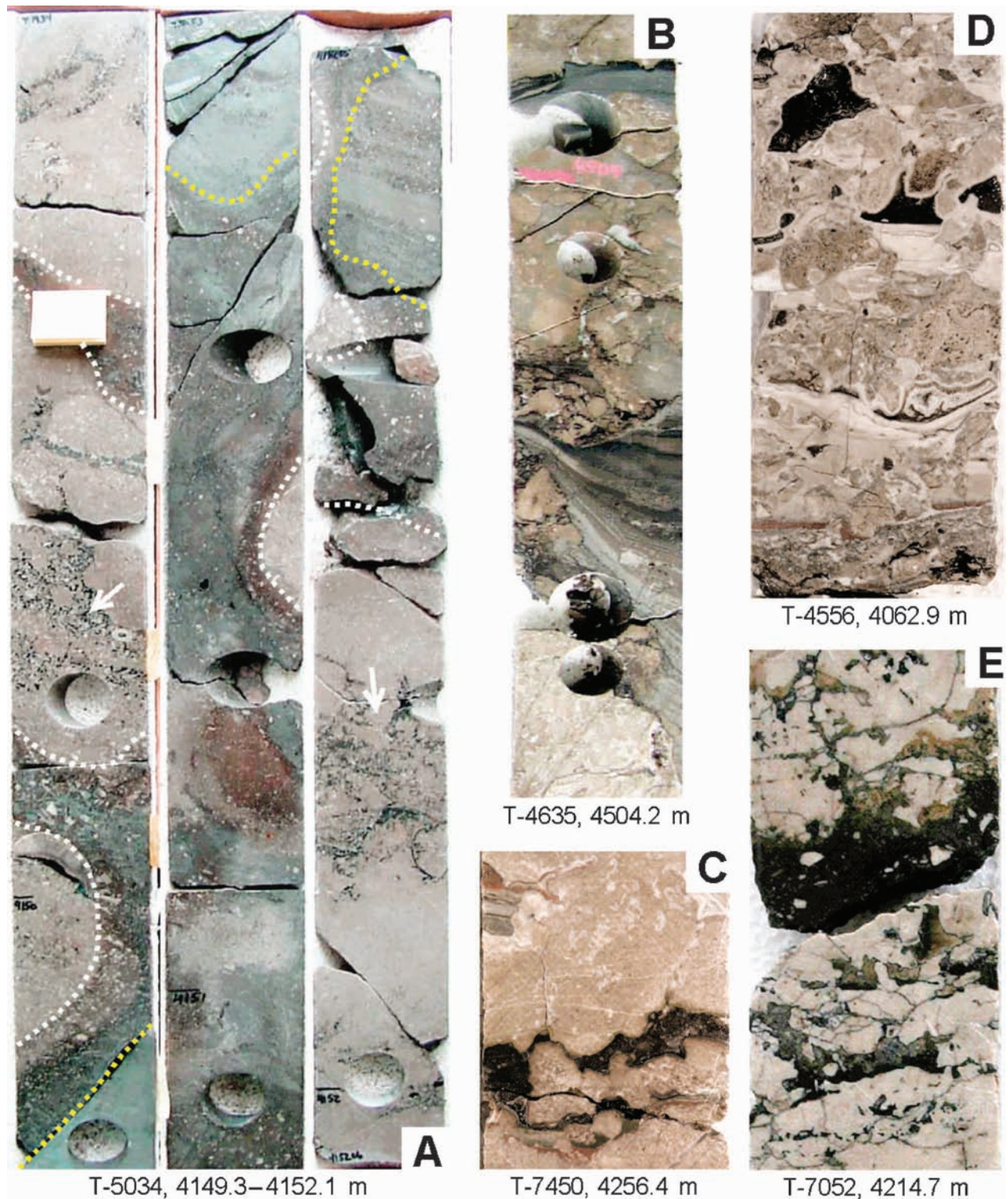


**FIGURE 29.** Core examples with sediment-filled features of possible karst origin. (A) Cavities filled with laminated, greenish-colored shale and carbonate formed in outer-platform crinoid skeletal packstone-rudstone. Cavity walls (yellow dashed lines) are surrounded by a zone of matrix corrosion and bitumen (white lines), but matrix reservoir quality overall is marginal. (B) Cavity developed in outer-platform to upper-slope boundstone filled with laminated green-gray marl and boundstone breccia. Because of the unique setting of the T-4635 well (see Figure 15A), this feature could be either a karst feature or a cavity that opened during rim detachment and subsequently filled in a deeper water setting. (C–E) Examples of smaller, geopetally filled fenestral cavities. The sediment fill sequence, which includes green and red clay (C and D), banded (marine) cement and cream-colored micrite (D), and dark-colored sediment (D and E), suggests a complex history of cavity formation and fill. All examples are associated with relatively poor matrix reservoir quality, however.

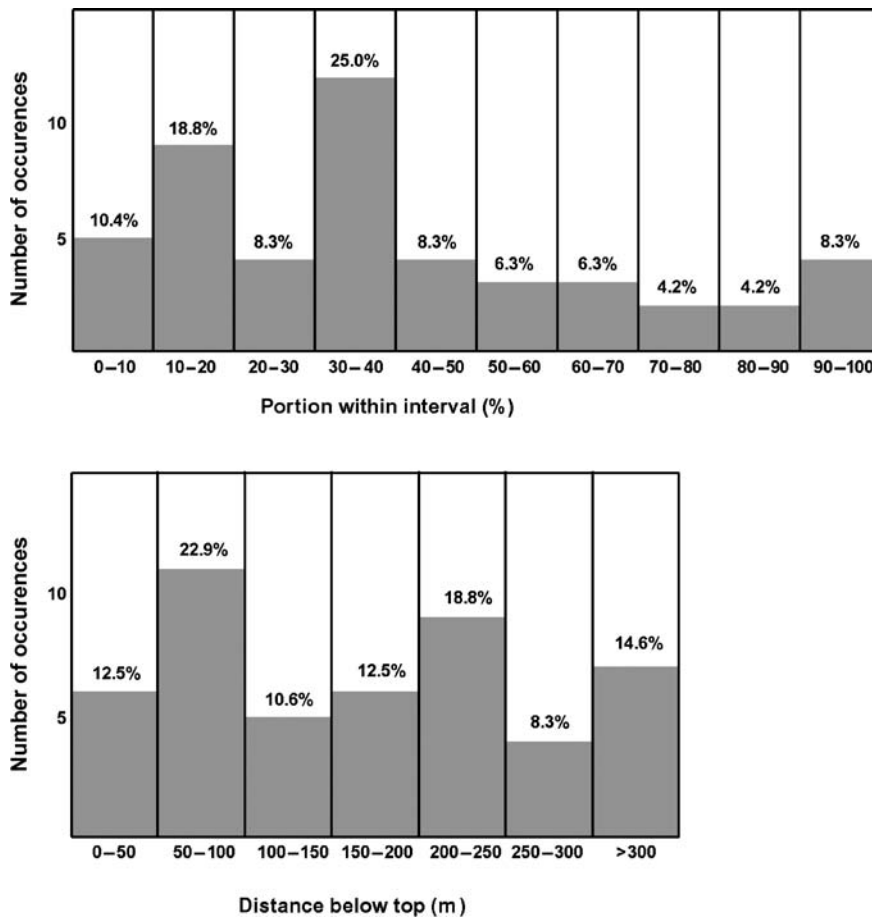


**FIGURE 30.** Distribution of lost circulation zones (LCZ) in the rim and flank. Most wells in the rim and flank have lost circulation somewhere in the reservoir section. The charts represent 48 LCZ in 13 wells (T-463, T-4346, T-4635, T-4556, T-5056, T-5059, T-5435, T-5454, T-5857, T-6261, T-6457, T-7252, and T-7453) that have been quantified by sustained loss rate, depth, and thickness. The distribution by distance in meters from the top of the section does not show a clear trend (left), but when the distribution is normalized to indicate relative proportion in the rim interval regardless of well position on the rim profile (right), the pattern supports anecdotal evidence that LCZ are more common in the upper part of the section, regardless of facies present there.

boundstones and tightly packed breccias have a greater fracture density compared to rudstones, packstones, and matrix-supported breccias, suggesting that lost circulation zones might be more common in upper- to middle-slope facies. However, based on well occurrences, it can be demonstrated that lost circulation zones are more common in the upper half to one-third and slightly more common near the base of the rim and flank section, regardless of position in the field (Figure 30). Such a distribution is inconsistent with a primary facies control on lost circulation and, like many other observations, points to a diagenetic overprint.

Current well spacing is still insufficient to clearly demonstrate geographical distribution patterns for lost circulation zones, a situation made even worse because most rim and flank wells drilled to date have encountered lost circulation somewhere in the reservoir section. More generally, facies in which fracture permeability was dominant compared to residual matrix permeability may be more prone to lost circulation because later dissolution was concentrated along fractures. Facies with higher residual matrix permeability (for example, poorly cemented

grainy facies and loosely packed breccias) may have allowed corrosive fluids to spread away from fractures and, thus, may ultimately prove less prone to lost circulation. This may be a reason why, in the transitional reservoir zone where permeable grainy facies are most abundant,

a relationship between lost circulation zones, bitumen, and corrosion is less obvious. Combined with reduced fracture density in the transitional reservoir zone, this factor may also be why lost circulation zones are less frequent in the outer platform region. Whatever diagenetic processes prove ultimately responsible for dissolution and lost circulation, their effects have produced a reservoir with large-scale interwell connectivity across the transitional reservoir zone, rim, and flank, despite a major stratal surface separating them and a complex facies distribution within each.

### SUMMARY AND CONCLUSIONS

Based on currently available data, the Tengiz rim and flank are interpreted to have accumulated in two stages. The early stage was dominated by instability and relatively continuous large-scale failure and mass wasting, resulting in deposition of debris aprons around the base of the buildup consisting of coarse boundstone breccias and grainy platform-derived sediments. In the second stage, a wedge consisting of shallow- and outer-platform facies, upper-slope

microbial boundstone, middle-slope boundstone breccia, and lower-slope breccia and platform-derived sediment prograded out over the early debris apron. This stage was more successful along the eastern margin of the buildup because of favorable platform profile geometry, or elevated microbial productivity, or reduced tectonic influence in those areas, or some combination of those factors. Along the western margin of the buildup, progradation was only locally or partially successful, and rim failure predominated throughout the Serpukhovian and Bashkirian.

This study does not provide a process-based, fully predictive model of the distribution of reservoir properties in the Tengiz outer platform, rim, and flank. It raises as many questions as it answers, and some critical uncertainties remain. Some conclusions have alternatives and will likely require modification or change as drilling continues. Future surprises are probable, and subsequent generations of models will no doubt be different from the present one in some manner. However, the following observations indicate factors that are likely to have a significant impact on reservoir quality and prediction in the rim and flank:

- 1) Reservoir quality is dominantly controlled by fractures and large-scale dissolution and is a function of earlier porosity destruction because of prebitumen cementation versus later dissolution associated with bitumen formation.
- 2) Porosity destruction caused by sediment infill and prebitumen cementation was significant and affected primary voids, early dissolution voids, early fractures, and early karst features. In particular, early fractures and large-scale dissolution features or karsts are largely filled and do not have a major impact on reservoir quality.
- 3) Corrosive dissolution and bitumen are a late-diagenetic overprint and are responsible for significant porosity modification in a wide variety of features including later fractures, microbial fabrics, micritic skeletal grains, breccia clasts, certain cements, and stylolites.
- 4) Facies control of fracture density results in both open and closed types being more common in mechanically rigid facies, such as microbial boundstone, cemented grainstone, and clast-supported breccia, and less abundant in facies such as rudstone, packstone, and matrix-supported breccia.
- 5) Lost circulation zones appear to be more commonly associated with solution-enlarged fractures than with vuggy intervals and are therefore likely controlled by either fracture distribution or the distribution of late dissolution fairways.
- 6) Enhanced matrix porosity caused by late dissolution and bitumen cement is commonly better developed where solution-enlarged fractures are present; however, extensive matrix corrosion may be associated with intervals that are less likely to produce severe lost circulation.
- 7) Reservoir-quality variability exists at large and small scales, resulting in considerable well-to-well differences in regions that are similar in terms of facies, stratigraphy, and depositional history. This suggests that facies is a weak secondary control on reservoir quality.

## ACKNOWLEDGMENTS

This study involved the work of a large group of geoscientists and specialists. The authors recognize the following individuals for insightful contributions to this manuscript: Kevin Nahm (Chevron), who believed early on that mechanically isotropic microbial boundstones could be mapped with seismic analysis; Brent Francis (ExxonMobil), who progressed this idea through development of the compaction model and who provided seismic interpretations for the debris apron concept; and Tom Heidrick (retired from Chevron), who engaged in valuable discussions regarding the minimal effects of early karst and the potential for later burial fractures. Wayne Narr (Chevron), Jim DeGraff (ExxonMobil), and Dan Carpenter (ExxonMobil) are acknowledged for building on this perception through rigorous description and analyses of fracture characteristics and distribution. Perhaps most importantly, Michael Clark (Chevron) is thanked for initiating an intense coring and core analysis program that formed the basis for most of our geologic studies and for his strong support of the sequence-stratigraphic framework.

We also gratefully thank the following individuals from ExxonMobil who made significant contributions of supporting data or data analysis: Gareth Jones and Yitian Xiao (numerical simulation of Tengiz diagenetic processes); Sean Guidry (fluid-inclusion analyses); Paul Hicks (temperature histories from basin modeling); Shin-Ju Ye and Peter Hillock (facies analysis of FMI logs). Early versions of the manuscript were improved by helpful reviews from Niall Toomey, Kelly Bergman, and Gareth Jones. Finally, we thank TengizChevroil and its shareholder companies for permission to publish this study.

## APPENDIX 1: RIM AND FLANK FACIES (MODIFIED FROM WEBER ET AL., 2003)

<i>Lithofacies and Microfacies</i>	<i>Description</i>	<i>Environment</i>
Crinoid-brachiopod skeletal rudstone to packstone	Medium-dark gray; large crinoids and/or fragmented thick-shelled brachiopods dominate; sometimes with microbial fabrics and cements	Deep subtidal outer platform, possibly below wave base; abundant in central to upper parts of late Visean and Serpukhovian outer-platform cycles
Outer platform breccias and conglomerates	Grainstone floatbreccia to packbreccia: light-medium brown; subangular to subrounded clasts of platform-derived grainstone and packstone; skeletal wackestone to grainstone matrix, sometimes with microbial fabrics and cements	Deep outer platform, possibly lowstand; basal parts of Serpukhovian outer-platform cycles
	Grainstone packbreccia: light brown, gray, and black; angular clasts of grainstone and rudstone with mixed lithofacies types	Shallow outer platform; lag or possibly karst? Tops of Serpukhovian outer-platform cycles
	Coral rudstone to conglomerate: medium brown to gray; colonial coral fragments; coarse-grained skeletal matrix with abundant crinoids	Shallow outer-platform; basal parts of Serpukhovian outer-platform cycles; possible patch-reef detritus
Brachiopod rudstone (coquina) to boundstone	Light gray-brown to medium brown-gray; brachiopod shell fragments and whole shells; some articulated, in feeding or growth position; abundant micritic matrix, some microbial fabrics and calcite cement; minor coarse skeletal debris, crinoids	Shallow outer-platform; basal parts of Serpukhovian outer-platform cycles; mud-mounds, mound detritus, and intermound deposits
Microbial boundstone	Type C (skeletal-micritic boundstone): light-medium brown, massive to peloidal with abundant fenestrae; crinoids, brachiopods, fenestellid bryozoans, algae, forams, and other skeletal grains bound together by clotted microbial fabric and multiple cement generations (as much as 50% cement)	Serpukhovian deep, subtidal, outer-platform to upper-slope platform break
	Type B (laminar-cemented boundstone): light brown; irregular concentric or wavy-aminated fabric consisting of microbial filaments and early cement (botryoidal, fibrous and radiaxial; inclusion rich; as much as 75%); minor skeletal grains, including fenestellid bryozoa, crinoids, ostracods, thin-walled pelecypods and forams	Serpukhovian upper slope
	Type A (peloidal-micritic boundstone): light gray-light brown; generally massive or featureless, with minor growth structures and abundant irregular fenestrae or tubules; clotted peloidal fabric and early cement (as much as 25%); sparse fauna, including fenestellid bryozoans, ostracods, and thin-walled pelecypods	Serpukhovian upper to middle slope

## APPENDIX 1: (CONT.)

<i>Lithofacies and Microfacies</i>	<i>Description</i>	<i>Environment</i>
Boundstone breccia	Welded to mosaic breccia: light-medium brown and gray; subangular centimeter- to meter-size clasts of upper-slope boundstone types; tight, clast-supported fabric, sometimes with stylolitic clast boundaries (welded breccia), sometimes with blocky calcite cement (mosaic breccia); minor platform-derived matrix (skeletal grains, large crinoids); occasional platform-derived grainstone or packstone lithoclasts	Serpukhovian upper to middle slope and debris apron
	Float- to packbreccia: light-dark brown and gray; subangular to subrounded, millimeter- to meter-size clasts of upper slope-derived boundstone types; grainstone-packstone matrix with platform-derived skeletal grains; large crinoids and fragmented brachiopod shells; occasional platform-derived grainstone or packstone lithoclasts	Serpukhovian middle to lower slope and debris apron
Crinoid-lithoclast rudstone-packstone	Brown-light gray; poorly to moderately sorted, crinoid-rich rudstone (platform-derived); fragmented brachiopod shells; sand-size skeletal grains and millimeter- to centimeter-size lithoclasts (upper slope and platform derived)	Serpukhovian middle to lower slope and debris apron
Skeletal-lithoclastic rudstone-grainstone-floatstone	Medium-dark gray; thin to thick bedded, wavy-bedded to laminated, graded; locally siliceous to slightly dolomitic; platform-derived grains (forams, crinoids, algae, brachiopods, crinoids); occasional millimeter- to centimeter-size boundstone or slope-derived clasts, volcanic siltstone or sandstone clasts	Serpukhovian lower slope and debris apron
Allochthonous grainstone	Light brown-medium gray; moderately sorted ooid or skeletal grainstone; massive to well bedded	Lower slope and debris apron; Serpukhovian and Bashkirian
Lime wackestone-mudstone	Brown, gray, and black; argillaceous, siliceous, and commonly dolomitic; thin laminated to thin bedded; sponge spicules, minor skeletal grains, and sparse radiolarians; commonly interbedded with volcanic silt and sand; potential source rock	Lower slope, debris apron and basal; Viséan, Serpukhovian, and Bashkirian

## APPENDIX 2: FLUID-INCLUSION RESULTS

Well	Depth (m)	Platform Sequence	Phase	Type	# incl.	$T_{homog}$ (Water) (°C)
T-4635	4466.25	Serpukhovian rim	Equant CC	Primary	2	85–90
T-4635	4466.25	Serpukhovian rim	Equant CC	Primary	2	90–95
T-4635	4482.63	Serpukhovian rim	Equant CC	Primary	1	88
T-4635	4482.63	Serpukhovian rim	Equant CC	Primary	3	80–85
T-4635	4482.63	Serpukhovian rim	Equant CC	Primary	2	85–90
T-4635	5055.25	Famennian	Calcite	Unspecified	5	105–110
T-4635	5055.25	Famennian	Calcite	Unspecified	6	105–115
T-4635	5055.25	Famennian	Calcite	Unspecified	>10	110–120
T-4635	5055.25	Famennian	Calcite	Unspecified	4	90–95
T-47	5392.5	Famennian	Quartz vein	Unspecified	No assemblage	115–125
T-5056	4194.2	Serpukhovian rim	Equant CC	Primary	1	80–85
T-5056	4194.2	Serpukhovian rim	Equant CC	Primary	5	85–90
T-5056	4200.47	Serpukhovian rim	Fluorite	Primary	4	110–125
T-5056	4200.47	Serpukhovian rim	Fluorite	Primary	4	110–125
T-5056	5453.55	Famennian	Zoned CC	Primary	2	100
T-5056	5453.55	Famennian	Zoned CC	Primary	3	95–100
T-5056	5453.55	Famennian	Equant CC	Unspecified	5	85–95
T-5056	5476.22	Famennian	Calcite	Primary	4	95–105
T-5857	4816.93	Serpukhovian rim	Prismatic CC	Primary	2	80–85
T-5857	4816.93	Serpukhovian rim	Prismatic CC	Primary	3	85–90
T-6337	4894.37	Visean D	Calcite	Primary	2	85–90
T-6337	4945.64	Visean D	Equant CC	Primary	4	85–90
T-6337	4945.64	Visean D	Equant CC	Primary	4	85–90
T-6337	4945.64	Visean D	Equant CC	Primary	3	85–90
T-8	3972	Bashkirian	Coarse CC	Unspecified	4	100–107
T-8	4044.5	Serpukhovian	Zoned CC	Primary	4	80–95
T-8	4044.5	Serpukhovian	Equant CC	Primary	2	85–95
T-8	4056.8	Serpukhovian	Equant CC	Primary	2	85–90

Data for hydrocarbon-water or vapor-filled inclusions:

Phase refers to cement types described in the text (see Figure 24). "Calcite" indicates the cement phase preceding bitumen formation and, in most cases, refers to equant calcite. Prismatic calcite represents the cores of zoned cement crystals (see Figure 20), and zoned calcite represents subsequent inclusion-rich growth zones (either calcite or dolomite). Coarse calcite is a postbitumen cement phase. An inclusion type of "unspecified" indicates an assemblage or train whose orientation was not specified during analysis, but was not designated as cutting across growth planes and may be primary. The column "# incl." indicates the number of individual inclusions in a train or assemblage.

## REFERENCES CITED

- Bahamonde, J. R., C. Vera, and J. R. Colmenero, 2000, A steep-fronted Carboniferous carbonate platform: Clinoformal geometry and lithofacies (Picos de Europa, NW Spain): *Sedimentology*, v. 47, p. 645–664.
- Blendinger, W., 2001, Triassic carbonate buildup flanks in the Dolomites, northern Italy: Breccias, boulder fabric and the importance of early diagenesis: *Sedimentology*, v. 48, no. 5, p. 919–933.
- Brenckle, P. L., and N. V. Milkina, 2003, Foraminiferal timing of carbonate deposition on the Late Devonian (Famennian)–middle Pennsylvanian (Bashkirian) Tengiz platform, Kazakhstan: *Revista Italiana di Paleontologia e Stratigrafia*, v. 109, no. 2, p. 131–158.
- Cander, H., 1995, Interplay of water-rock interaction efficiency, unconformities, and fluid flow in a carbonate aquifer: Floridan aquifer system, in D. A. Budd, A. H. Saller, and P. M. Harris, eds., *Unconformities and porosity in carbonate strata: AAPG Memoir 63*, p. 103–124.
- Choquette, P. W., and N. P. James, 1987, Introduction, in N. P. James and P. W. Choquette, eds., *Paleokarst*: New York, Springer-Verlag, p. 1–21.
- Della Porta, G., J. A. M. Kenter, J. R. Bahamonde, A. Immenhauser, and E. Villa, 2003, Microbial boundstone

- dominated carbonate slope (Upper Carboniferous, N Spain): Microfacies, lithofacies distribution and stratal geometry: *Facies*, v. 49, p. 175–208.
- Esteban, M., and J. L. Wilson, 1993, Introduction to karst systems and paleokarst reservoirs, *in* R. D. Fritz, J. L. Wilson, and D. A. Yurewicz, eds., *Paleokarst related hydrocarbon reservoirs: SEPM Core Workshop 18*, p. 1–9.
- Ford, D. C., 1995, Paleokarsts as a target for modern karstification: *Carbonates and Evaporites*, v. 10, no. 2, p. 138–147.
- Heydari, E., 2000, Porosity loss, fluid flow and mass transfer in limestone reservoirs: Application to the Upper Jurassic Smackover Formation, Mississippi: *AAPG Bulletin*, v. 84, no. 1, p. 100–118.
- Hill, C. A., 1987, *Geology of Carlsbad Cavern and other caves in the Guadalupe Mountains: New Mexico Bureau of Mines and Mineral Resources, New Mexico and Texas Bulletin 117*, 150 p.
- Hill, C. A., 1990, Sulfuric acid speleogenesis of Carlsbad Cavern and its relationship to hydrocarbons, Delaware basin, New Mexico and Texas: *AAPG Bulletin*, v. 74, no. 11, p. 1685–1694.
- Hill, C. A., 1995, H<sub>2</sub>S-related porosity and sulfuric acid oil-field karst, *in* D. A. Budd, A. H. Saller, and P. M. Harris, eds., *Unconformities and porosity in carbonate strata: AAPG Memoir 63*, p. 301–313.
- Jones, G. D., F. F. Whitaker, P. L. Smart, and W. E. Sanford, 2004, Numerical analysis of seawater circulation in carbonate platforms: II. The dynamic interaction between geothermal and brine reflux circulation: *American Journal of Science*, v. 304, p. 250–284.
- Kenter, J. A. M., P. M. Harris, and G. Della Porta, 2005, Steep microbial boundstone-dominated platform margins—Examples and implications: *Sedimentary Geology*, v. 178, p. 5–30.
- Kenter, J. A. M., P. M. Harris, J. F. Collins, L. J. Weber, G. Kuanysheva, and D. J. Fischer, 2006, Late Viséan to Bashkirian platform cyclicity in the central Tengiz buildup, Precaspian Basin, Kazakhstan: Depositional evolution and reservoir development, *in* P. M. Harris and L. J. Weber, eds., *Giant hydrocarbon reservoirs of the world: From rocks to reservoir characterization and modeling: AAPG Memoir 88/SEPM Special Publication*, p. 7–54.
- Kerans, C., and P. M. Harris, 1993, Outer shelf and shelf crest, *in* D. G. Bebout and C. Kerans, eds., *Guide to the Permian reef geology trail, McKittrick Canyon, Guadalupe Mountains National Park, west Texas, Guidebook 26: Austin, Bureau of Economic Geology*, p. 32–43.
- Kerans, C., N. F. Hurley, and P. E. Playford, 1986, Marine diagenesis in Devonian reef complexes of the Canning basin, Western Australia, *in* J. H. Schroeder and B. H. Purser, eds., *Reef diagenesis: Berlin, Springer-Verlag*, p. 357–380.
- Kirkland, B. L., J. A. D. Dickson, R. A. Wood, and L. S. Land, 1998, Microbialite and microstratigraphy: Encrustations in the middle and upper Capitan Formation, Guadalupe Mountains, Texas and New Mexico, U.S.A.: *Journal of Sedimentary Research*, v. 68, p. 956–969.
- Kohout, F. A., H. R. Henry, and J. E. Banks, 1977, Hydrology related to geothermal conditions of the Floridan Plateau, *in* K. L. Smith and G. M. Griffin, eds., *The geothermal nature of the Floridan Plateau: Florida Department of Natural Resources Bureau Geology Special Publication 21*, p. 1–34.
- Lisovsky, N. N., G. N. Gogonenkov, and Y. A. Petzoukha, 1992, The Tengiz oil field in the Pre-Caspian Basin of Kazakhstan (former USSR)—Supergiant of the 1980s, *in* M. T. Halbouty, ed., *Giant oil and gas fields of the decade 1978–1988: AAPG Memoir 54*, p. 101–122.
- Lucia, F. J., 1995, Lower Paleozoic cavern development, collapse, and dolomitization, Franklin Mountains, El Paso, Texas, *in* D. A. Budd, A. H. Saller, and P. M. Harris, eds., *Unconformities and porosity in carbonate strata: AAPG Memoir 63*, p. 279–300.
- Lucia, F. J., 1999, *Carbonate reservoir characterization: New York, Springer-Verlag*, 222 p.
- Machel, H. G., 1987, Some aspects of diagenetic sulphate-hydrocarbon redox reactions, *in* J. D. Marshall, ed., *Diagenesis of sedimentary sequences: Geological Society (London) Special Publication 36*, p. 15–38.
- Machel, H. G., 1989, Relationships between sulphate reduction and oxidation of organic compounds to carbonate diagenesis, hydrocarbon accumulations, salt domes, and metal sulphide deposits: *Carbonates and Evaporites*, v. 4, no. 2, p. 137–151.
- Machel, H. G., and J. H. Anderson, 1989, Pervasive subsurface dolomitization of the Nisku Formation in central Alberta: *Journal of Sedimentary Petrology*, v. 59, no. 6, p. 891–911.
- Melim, L. A., and P. A. Scholle, 1995, The forereef facies of the Permian Capitan Formation: The role of supply versus sea-level changes: *Journal of Sedimentary Research*, v. B65, no. 1, p. 107–118.
- Morrow, D. W., 1998, Regional subsurface dolomitization: Models and constraints: *Geoscience Canada*, v. 25, p. 57–70.
- Myroie, J. E., and J. L. Carew, 1995, Karst development on carbonate islands, *in* D. A. Budd, A. H. Saller, and P. M. Harris, eds., *Unconformities and porosity in carbonate strata: AAPG Memoir 63*, p. 55–76.
- Playford, P. E., 1984, Platform-margin and marginal-slope relationships in Devonian reef complexes of the Canning basin, *in* P. G. Purcell, ed., *The Canning basin, Western Australia: Geological Society of Australia and Petroleum Exploration Society of Australia, Canning basin Symposium, Perth 1984*, p. 189–234.
- Ross, C. A., and J. R. P. Ross, 1987, Late Paleozoic sea levels and depositional sequences: Cushman Foundation for Foraminiferal Research Special Publication 24, p. 137–149.
- Ross, C. A., and J. R. P. Ross, 1988, Late Paleozoic transgressive-regressive deposition, *in* C. K. Wilgus, B. S. Hastings, C. Kendall, H. W. Posamentier, C. A. Ross, and J. C. Van Wagoner, eds., *Sea-level changes:*

- An integrated approach: SEPM Special Publication 42, p. 227–247.
- Saller, A. H., 1984, Petrologic and geochemical constraints on the origin of subsurface dolomite, Enewetak Atoll: An example of dolomitization by normal sea water: *Geology*, v. 12, p. 217–220.
- Sanford, W. E., F. F. Whitaker, P. L. Smart, and G. D. Jones, 1998, Numerical analysis of seawater circulation in carbonate platforms: I. Geothermal circulation: *American Journal of Science*, v. 298, p. 801–828.
- Stephens, N. P., and D. Y. Sumner, 2003, Famennian microbial reef facies, Napier and Oscar Ranges, Canning basin, Western Australia: *Sedimentology*, v. 50, p. 1283–1302.
- Stoessell, R. K., 1992, Effects of sulfate reduction on  $\text{CaCO}_3$  dissolution and precipitation in mixing-zone fluids: *Journal of Sedimentary Petrology*, v. 62, no. 5, p. 873–880.
- Tinker, S., 1998, Shelf-to-basin facies distributions and sequence stratigraphy of a steep-rimmed carbonate margin: Capitan depositional system, McKittrick Canyon, New Mexico and Texas: *Journal of Sedimentary Research*, v. 68, p. 1146–1174.
- Tinker, S. W., J. R. Ehrets, and M. D. Brondos, 1995, Multiple karst events related to stratigraphic cyclicity: San Andres Formation, Yates field, West Texas, *in* D. A. Budd, A. H. Saller, and P. M. Harris, eds., *Unconformities and porosity in carbonate strata: AAPG Memoir 63*, p. 213–237.
- Wagner, P. D., D. R. Tasker, and G. P. Wahlman, 1995, Reservoir degradation and compartmentalization below subaerial unconformities: Limestone examples from west Texas, China, and Oman, *in* D. A. Budd, A. H. Saller, and P. M. Harris, eds., *Unconformities and porosity in carbonate strata: AAPG Memoir 63*, p. 301–313.
- Weber, L. J., B. P. Francis, P. M. Harris, and M. Clark, 2003, Stratigraphy, lithofacies, and reservoir distribution, Tengiz field, Kazakhstan, *in* W. M. Ahr, P. M. Harris, W. A. Morgan, and I. D. Somerville, eds., *Permo-Carboniferous carbonate platforms and reefs: SEPM Special Publication 78 and AAPG Memoir 83*, p. 351–394.
- Wendte, J., H. Qing, J. Dravis, S. L. O. Moore, L. D. Stasiuk, and G. Ward, 1998, High temperature saline (thermo-flux) dolomitization of Swan Hills platform and bank carbonates, Wild River area, west-central Alberta: *Bulletin of Canadian Petroleum Geology*, v. 46, p. 210–266.

